# Electronic Supplementary Information

## All-Around Supramolecular Zwitterionic Hydrogel Electrolytes Enabling Environmentally Adaptive Dendrite-Free Aqueous Zinc Ion Capacitors

*Qingjin Fu[1], Sanwei Hao[1], Xinrui Zhang[1], Haonan Zhao[1], Feng Xu[1], and Jun Yang[1,2*]*

[1]Beijing Key Laboratory of Lignocellulosic Chemistry, College of Materials Science and Technology, Beijing Forestry University, Beijing 100083, China.

[2]State Key Laboratory of Pulp and Paper Engineering, South China University of Technology, Guangzhou 510640, China.

*E-mail: yangjun11@bjfu.edu.cn  Tel: 86-10-62337223

# Table of Contents

## Section S1 Supplementary Experimental Procedures

### Materials

Betaine, dimethylglycine, L-proline, sarcosine, TMAO, AA, $ZnSO_4 \cdot 7H_2O$, EG, Irgacure 2959, N,N′-methylene bis(acrylamide) (MBA), poly-(vinylidene fluoride) (PVDF), 1-methyl-2-pyrrolidone (NMP) are obtained from Beijing Lan Yi Co., Ltd. CNF aqueous suspension (approximately 5.0 wt%) is purchased from Tianjin University of Science and Technology.

### Preparation of CP/EGZn/zwitterion hydrogel electrolytes

AA is purified by passing through a basic alumina column to remove inhibitors. The reaction precursor is prepared by mixing AA and zwitterion (molar ratio, AA: zwitterion = 1:1) with Irgacure 2959 as photoinitiator (1:500 molar ratio to the monomer) and MBA as crosslinker (1:4000 molar ratio to the monomer) in the electrolytes that are obtained by dissolving $ZnSO_4 \cdot 7H_2O$ into the EG-CNF solvents (volume ratio, CNF:EG = 1:0.5) to form a $Zn^{2+}$ salt solution of 2 mol $L^{-1}$. The precursor is then poured into homemade PTFE molds and polymerized by 360 nm UV irradiation for 30 min (**Figure S62,S63**).

### Preparation of CP/EGZn/zwitterion hydrogel electrolyte-based ZICs

Activated Carbon (AC) positive electrodes are prepared by blading the mixture of commercially available AC (Cabot), carbon black (Cabot) and PVDF binder in a weight ratio of 8:1:1 in NMP solvent on carbon cloth (thickness: 0.36 mm) and then drying overnight in a vacuum oven at 60 °C. A strip of zinc sheet (thickness of 0.1 mm, purity >99.99%) is cut and washed with acetone before using as the negative electrode. The CP/EGZn/zwitterion hydrogel electrolyte-based ZIC is fabricated by sandwiching a CP/EGZn/zwitterion hydrogel electrolyte (thickness: about 1 mm) between a Zn foil (contact area with hydrogel electrolyte 1 cm[2)] and an activated carbon-loaded carbon cloth (contact area with hydrogel electrolyte 1 cm[2]) (**Figure S62,S64**). ZICs for the demo purpose are assembled by sandwiching a CP/EGZn/betaine hydrogel electrolyte (around 1 mm thickness) between a Zn foil (contact area with hydrogel electrolyte 3 cm[2]) and an activated carbon-loaded carbon cloth (contact area with hydrogel electrolyte 3 cm[2]).

**Materials characterization**

Morphology characterization of dried gels and Zn anode was made using a field-emission scanning electron microscopy (SEM, Hitachi SU8010). The interfacial microscopic images of the cross-section of assembled ZICs were obtained by an optical microscope (OLYMPUS BX43). The FT-IR spectroscopy analysis was conducted by using a Bruker Tensor II ATR-FTIR spectrometer. The transparency of the hydrogel film was evaluated with a UV–Visible spectrophotometer (UV-2550, Shimadzu). Nuclear magnetic resonance (NMR) was measured on Bruker 400M. Thermogravimetry analysis (TGA) was performed on DTG-60 via scanning a temperature range from 30 to 600 °C under $N_2$ (heating rate = 10 °C min$^{-1}$). The size distributions of saturated betaine solution, AA/$H_2O$, AA/betaine/$H_2O$, AA/betaine/ CNF, AA/betaine/EG, and AA/betaine/$ZnSO_4$ solutions were determined by DLS (Brookhaven Omini).

**Details for mechanical measurements**

The mechanical measurements of the hydrogels were carried out on a universal testing machine (Zwell/Roell) with a 200 N load cell at a constant velocity of 100 mm min$^{-1}$. The hydrogels were molded into rectangular specimens (10 mm in width, 5 mm in thickness, and 35 mm in length) and cylindrical specimens (25 mm height and 20 mm diameter) for tensile and compression testing, respectively. For cycle tensile test, the hydrogel was first stretched to a fixed strain (1000%) at a velocity of 100 mm min$^{-1}$ and then unload immediately at the same speed. Without interval waiting, the samples were subjected to the next cycle test. The Young's modulus was calculated from the slope of the initial linear region of the stress-strain curves (5-15% strain). Toughness was estimated by the area under the stress-strain curves until fracture point. For cycle compressive test, the specimen was initially compressed to a predetermined strain (60%) and then unloaded at the constant velocity (100 mm min$^{-1}$) at room temperature. Then, the successive loading-unloading compressive tests were conducted for twenty cycles without intervals between consecutive cycles. The dissipated energies were calculated from the area between loading-unloading curves. The stress relaxation measurements with the strain of 300%.

The puncture resistance tests were conducted on a universal testing machine (Zwell/ Roell) by using the sample-holding apparatus and needle shown in the picture below. The thickness of the samples was approximately 1 mm. The force and displacement were recorded by the universal testing machine. The puncture energy ($\Gamma$) was estimated by the area under the force-displacement curves until fracture point.

To investigate the mechanical performance of the hydrogels at low/high-temperature conditions, the samples were incubated under −40, −20, 0, 20, 40, 60, and 80 °C for at least 12 h. Then, the mechanical performance of these samples under different conditions was immediately examined after the samples were taken out. The low and high temperature were achieved via an ultra-low freezer (Thermo Scientific Forma 900) and oven, respectively.

**Details for adhesion measurements**

The adhesion strength and adhesion energy were quantified by the standard lap-shear test and the standard 180-degree peeling test at a constant peeling rate of 20 mm min$^{-1}$ using a universal test machine (Zwell/Roell), respectively. Samples for measurement of adhesion strength and adhesion energy were all normalized to 25 mm × 25 mm, and laminated between two substrates (i.e., Zn, Al, Cu, Ti, Ni, carbon cloth, and CNT paper), followed by preloading 1 kg weight for 10 min under ambient conditions. The adhesion strength was calculated by dividing the maximum force by the adhesion area. The adhesion energy was calculated by dividing the double plateau force by the sample width. Additionally, the adhesion-strip cyclic tests were also conducted to evaluate the effect of a cycle load on the adhesion strength and adhesion energy of the hydrogels. The long-term adhesiveness was characterized as a function of storage time on the adhesion strength and adhesion energy of the hydrogels.

For temperature-resistant adhesion, the hydrogels were initially sandwiched by the substrates (Zn-carbon and pigskin) and then incubated under −40, −20, 0, 20, 40, 60 and 80 °C for at least 12 h. At least three parallel samples were tested for each group.

**Details for anti-freezing and moisture-preserving measurements**

Differential scanning calorimetry (DSC) heating and cooling curves were collected using TA DSC250 scanning from −80 to 100 °C at a scanning rate of 10 °C min⁻¹ under nitrogen flow, which determined freezing point of hydrogels. The hydrogel samples (2 cm in diameter and 0.5 cm in height) were stored in the atmosphere (35~50% RH and 20~25 °C) for 10 days. The weight retention was calculated by dividing the weight of the hydrogel at different times by the initial weight of the hydrogel.

**Details for electrochemical measurements**

The Zn||Zn symmetric cells were assembled by sandwiching the hydrogel electrolytes between two Zn foils with thickness of 0.1 mm using CR2032 coin-type cells. The galvanostatic charge/discharge (GCD) measurements of the Zn||Zn symmetric cells with different hydrogel electrolytes were evaluated on a LAND CT2001A battery testing system. Linear polarization (LP) curve, chronoamperometry (CA), linear scanning voltammetry (LSV), and cyclic voltammetry (CV) curve were conducted in a three-electrode cell set-up using the electrochemical workstation (Autolab), where for LP and CA, the working electrode and the counter electrode both were Zn foils, and the reference electrode was Ag/AgCl electrode, and for LSV and CV, Ti foil was used as the working electrode, Zn plate as the counter and reference electrode. The corrosion rate of Zn foil in different electrolytes was quantified according to the corrosion potential and corrosion current that calculated from Tafel fit system in electrochemical workstation (Autolab). The efficiency of protection ($\eta\%$) for Zn electrodes in a CP/EGZn/zwitterion was calculated by using the values of the corrosion current $I_{corr}$ shown as the **Eq. 1**:[1]

$$\eta\% = \left(\frac{I_{corr(CP/EGZn)} - I_{corr(CP/EGZn/zwitterion)}}{I_{corr}}\right) \times 100\% \tag{1}$$

Assume that the relationship between critical Zn nuclei radius ($r_{crit}$) and nucleation overpotential (NOP) obeyed the **Eq. 2**:[2]

$$\gamma_{crit} = 2\frac{\Upsilon V_m}{F|\eta|} \tag{2}$$

where $\Upsilon$ is the surface energy of the Zn-electrolyte interface, $V_m$ is the molar volume of Zn, $F$ is Faraday's constant, and $\eta$ is the NOP.

Zn$^{2+}$ transference number ($t_{Zn}^{2+}$) was measured in the Zn‖Zn symmetric cells with different hydrogel electrolytes by using DC polarization combined with AC impedance at room temperature. To confirm the migration of Zn$^{2+}$, $t_{Zn}^{2+}$ is calculated by **Eq. 3**:

$$t_{Zn^{2+}} = \frac{R_{cell}}{R_{DC}}$$

(3)

where $R_{cell}$ was the total cell resistance before polarization, $R_{DC} = V_{DC}/I_{DC}$, and $V_{DC}$ was the applied potential, $I_{DC}$ was the stable current.

The ionic conductivities of the SZHEs were measured by the electrochemical impedance spectroscopy (EIS) using an electrochemical workstation (Autolab) operated in the frequency range of 0.01 to $10^5$ Hz and the amplitude of 5 mV. The samples were sandwiched between two stainless steel electrodes (SS) and incubated under a variety of temperatures of −40, −20, 0, 20, 40, 60, and 80 °C for at least 12 h, for the measurement. The ionic conductivities (σ) of the SZHEs were calculated by **Eq. 4**:

$$\sigma = \frac{L}{RS}$$

(4)

where $L$ represents the thickness of electrolyte, $S$ is the area of the electrolyte, and $R$ is the bulk resistance obtained from the intercept at the real part in Nyquist plots.

All electrochemical performances (CV, GCD, and EIS) of our assembled zinc ion capacitors (ZICs) were performed by an electrochemical workstation (Autolab) using two-electrode cells with 0.1-mm-thick Zn foils (1 cm$^2$) as negative electrodes and AC-loaded carbon cloth (1 cm$^2$) with 1 mg solid materials (0.8 mg AC) as positive electrodes, together with 1-mm-thick CP/EGZn/zwitterion gel electrolytes (1 cm$^2$). Long term stability tests were conducted by a battery testing system (LANHE).

The specific gravimetric capacitance ($C$, F g$^{-1}$) of assembled ZICs was calculated from GCD curves according to **Eq. 5**:

$$C = \frac{It}{mU}$$

(5)

where $I$ is the current density, $t$ is the discharging time, $m$ is the mass loading of AC (approximately 0.8 mg cm$^{-2}$ active material in each tested ZIC), and $U$ is the voltage difference of the discharge curve.

The energy density ($E$) and power density ($P$) of assembled ZICs were calculated based on the following **Eq. 6** and **Eq. 7**:

$$E = \frac{1}{2 \times 3.6} C \times V^2 \qquad (6)$$

$$P = \frac{E}{t} \qquad (7)$$

where $C$ is the specific gravimetric capacitance of AC used in each device, $V$ is the working voltage window.

**Density functional theory (DFT)**

All the computations were conducted by adopting the QUICKSTEP program as implemented in the CP2K package, which used a mixed Gaussian and plane wave scheme with the wave functions expanded in terms of a Gaussian basis set and the charge density represented with an auxiliary plane wave basis.

We employed DZVP-MOLOPT-GTH basis sets, a 600 Ry cutoff for the auxiliary plane wave expansion of the charge density, and Goedecker-Teter-Hutter (GTH) norm-conserving pseudopotentials to represent the core electrons. The calculations were conducted using the generalized gradient approximation and the Perdew-Burke-Ernzerhof (PBE) functional. Ab initio molecular dynamics (AIMD) were used in this work. The dynamics was run with the NVT ensemble using a Nose thermostat with a damping parameter of 0.5 at a temperature of 330 K. All AIMD simulations were run for 2 ps to obtain accurate statistics of the electrode–surface and electrode–solvent interactions. The binding energy can be calculated by the equation: $E_{binding} = E_{slab+x} - E_{slab} - E_x$, where the $E_{slab+x}$ is the energy of systems with adsorbate, $E_{slab}$ the systems without Li atom, $E_x$ is the adsorbate.
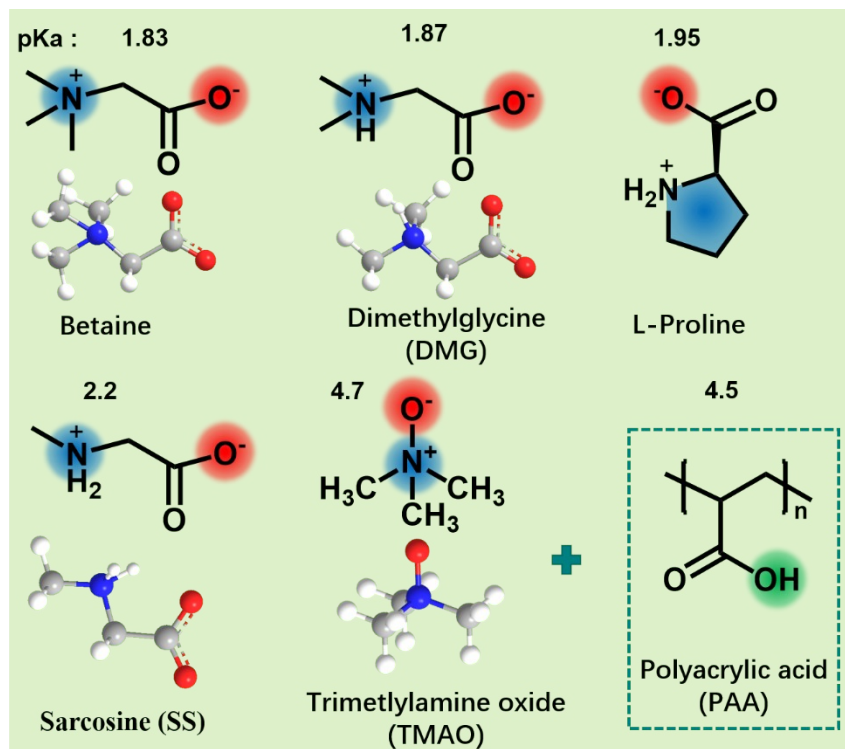
# Section S2 Supplementary Figures



**Figure S1.** Molecular structures of zwitterions and polyacrylic acid (PAA) for the preparation of the SZHE.
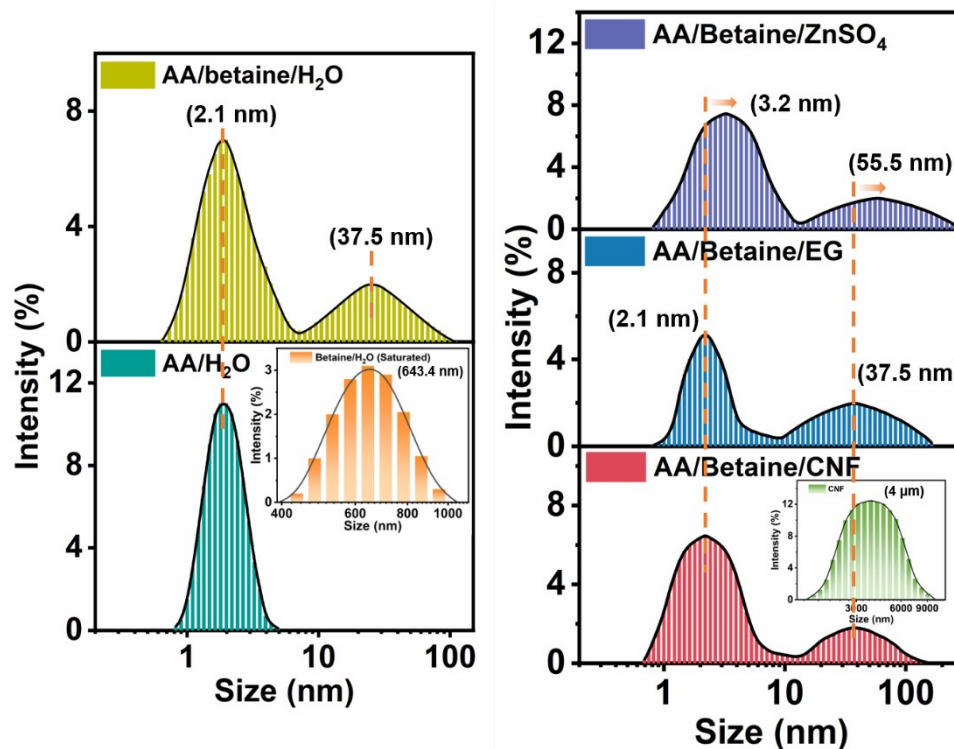
**Figure S2.** DLS size distribution curves of saturated betaine solution, AA/H$_2$O, AA/ betaine/H$_2$O, AA/betaine/CNF, AA/betaine/EG, and AA/betaine/ZnSO$_4$ solutions.

Note that high-concentration zwitterions like betaine and TMAO in water would form chain-like aggregation due to the electrostatic interactions between negatively charged carboxylate/oxygen and positively charged nitrogen (***J. Mol. Liq.* 2020, 318, 114253; *Nat. Commun.*, 2021, 12, 4082; *Adv. Funct. Mater.* 2022, 32, 2207140**).To evidence the presence of the supramolecular zwitterion network, we performed the dynamic light scattering (DLS) analysis of saturated betaine solution, AA/H$_2$O, AA/betaine/ H$_2$O, AA/ betaine/CNF, AA/betaine/EG, and AA/betaine/ZnSO$_4$ reaction precursors, respectively. As shown in **Figure S2**, there are two peaks in the reaction precursor; the size at 2.1 nm is ascribed to AA clustering via H-bonds, and the size at 37.5 nm should arise from betaine clustering, which is much smaller than that in saturated betaine solution (centered at 643.4 nm) due to AA-induced pH decrease (***Nat. Commun.*, 2021, 12, 4082**). Additionally, we found that the incorporation of CNF (centered at 4 μm) or EG makes no influence on the size of AA clustering and betaine clustering, whereas the size of AA clustering and betaine clustering increases significantly after chelating with ZnSO$_4$, which may be because the chelation of zinc and AA and betaine forms the tighter supramolecular network structure, and thereby results in a more concentrated size distribution of AA clustering and betaine

clustering (*Food Chem.* **2021, 347, 129043**). Thus, the supramolecular zwitterion network of AA/betaine/H$_2$O, AA/betaine/CNF, AA/betaine/EG, and AA/betaine/ZnSO$_4$ is well maintained within the CP/EGZn/betaine hydrogel, which is the source of excellent mechanical property.
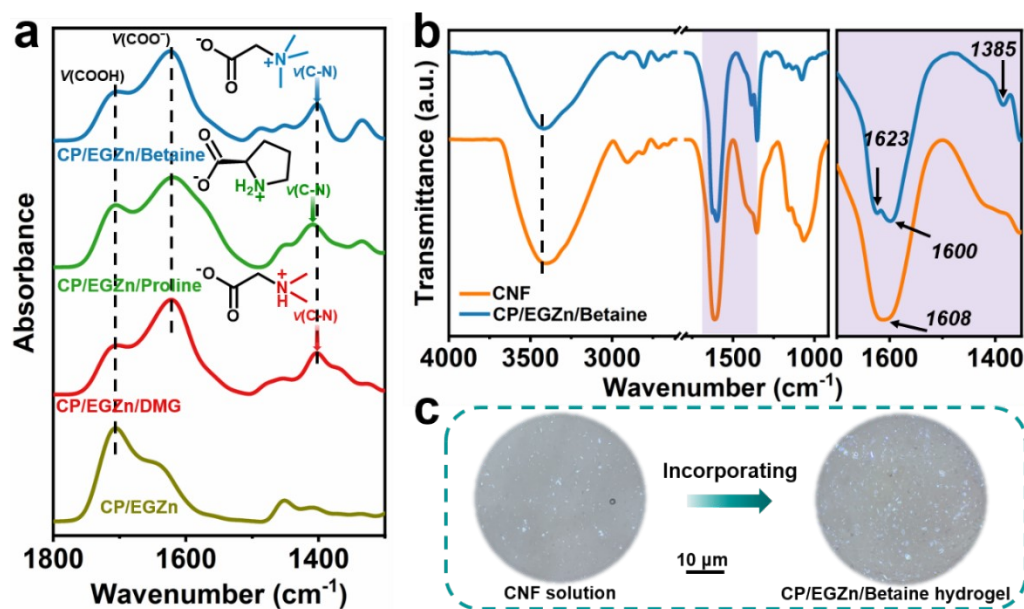


**Figure S3.** (a) ATR-FTIR spectra and assignments of the CP/EGZn hydrogels and the CP/EGZn/zwitterion hydrogels. (b) FT-IR spectra of the CNF and CP/EGZn/betaine hydrogel. (c) Optical microscopic images of the CNF solution and CP/EGZn/betaine hydrogels (The CNF as represented by the white crystalline).

Molecular structures of the as-prepared CP/EGZn/zwitterion hydrogels are examined using ATR-FTIR spectroscopy (**Figure S3a**). The FTIR spectrum of CP/EGZn/zwitterion hydrogels exhibits three clear peaks at 1623 and 1402 cm$^{-1}$ (Noting that 1409 cm$^{-1}$ for proline) for $v$(COO$^-$) and $v$(C–N), respectively, and the peak at 1708 cm$^{-1}$ corresponds to $v$(C = O) of PAA in the CP/EGZn hydrogel.

The FT-IR spectra of the CNF and CP/EGZn/betaine hydrogels are also recorded (**Figure S3b**). The peak at 1608 cm$^{-1}$ corresponding to C=O stretching vibration of the salt form of carboxylate groups in neat CNF sample shifts to the lower wavenumbers (1600 cm$^{-1}$) after the incorporating into P/EGZn/betaine hydrogels. This is attributed to the metal-carboxylate coordination between the carboxyl groups of the CNF and Zn$^{2+}$ in the resultant CP/EGZn/betaine hydrogel. Additionally, the optical microscope is performed on the CNF solution and CP/EGZn/betaine hydrogels to visualize the CNF distribution. As displayed in **Figure S3c**, the CNF with the white crystalline achieves a uniform distribution in the CP/EGZn/betaine hydrogel, which

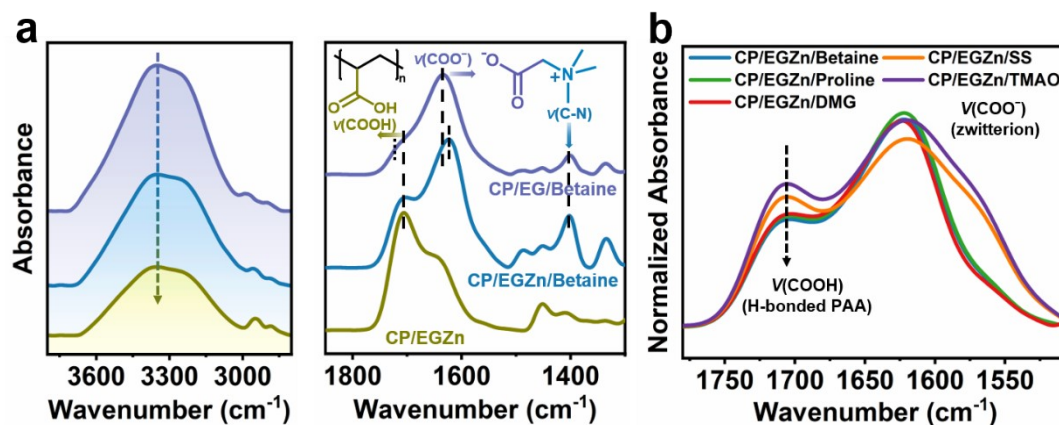would be significantly beneficial for the mechanical reinforcement.



**Figure S4.** (a) ATR-FTIR spectra and assignments of the CP/EGZn, CP/EGZn/betaine, and CP/EG/betaine hydrogel. (b) Normalized ATR-FTIR spectra of the CP/EGZn/ zwitterion hydrogel.

To validate the internal interactions in the representative CP/EGZn/betaine hydrogel, the ATR-FTIR spectra of CP/EGZn, CP/EGZn/betaine, and CP/EG/betaine are compared in **Figure S4a**. Compared to that of CP/EG/betaine, the clear peaks of the CP/EGZn/betaine hydrogels at 1623 and 1708 cm$^{-1}$ for $v(COO^-)$ and $v(C = O)$ shift to the higher wavenumbers, which reveal the ionic complexation between $Zn^{2+}$ and $v(C = O)$ from PAA and $v(COO^-)$ from betaine.

The relative amount of $v(COOH)$ (H-bonded PAA) as normalized by the spectral intensity of $v(COO^-)$ (zwitterion) increases in the order of betaine, proline, and DMG, corresponding to the formation of more H-bonded crosslinks (**Figure S4b**). This order is in full accordance with the increment of the initial moduli of CP/EGZn/zwitterion hydrogels (**Figure S12b**), which may result from the reduced zwitterion-PAA interactions in the case of tertiary and secondary amines with a lower electropositivity.[3]
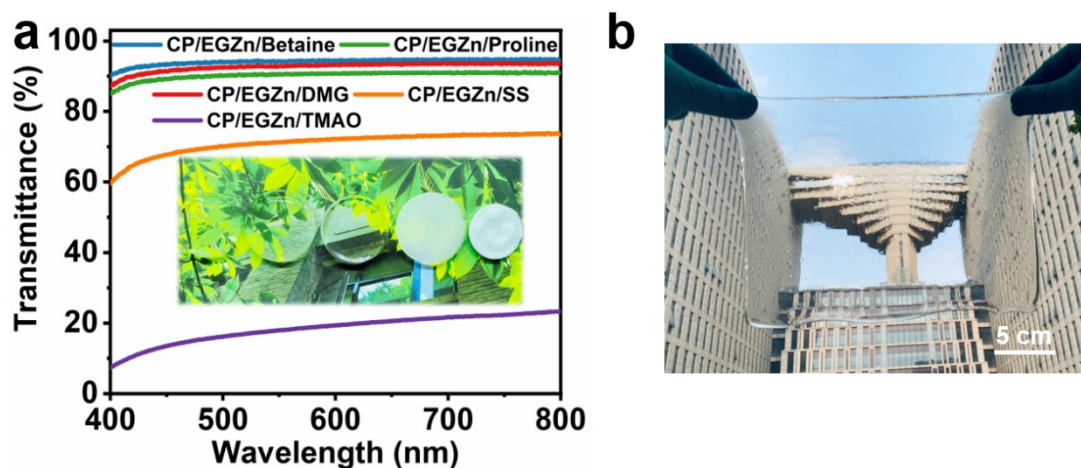
**Figure S5.** UV-Vis transmittance spectrum of the CP/EGZn/zwitterion hydrogel with a thickness of 1 mm. Inset: photographs of the CP/EGZn/zwitterion hydrogel (Betaine, Proline, DMG, SS, and TMAO from left to right)). b) Optical image of the large-sized CP/EGZn/betaine hydrogel film.
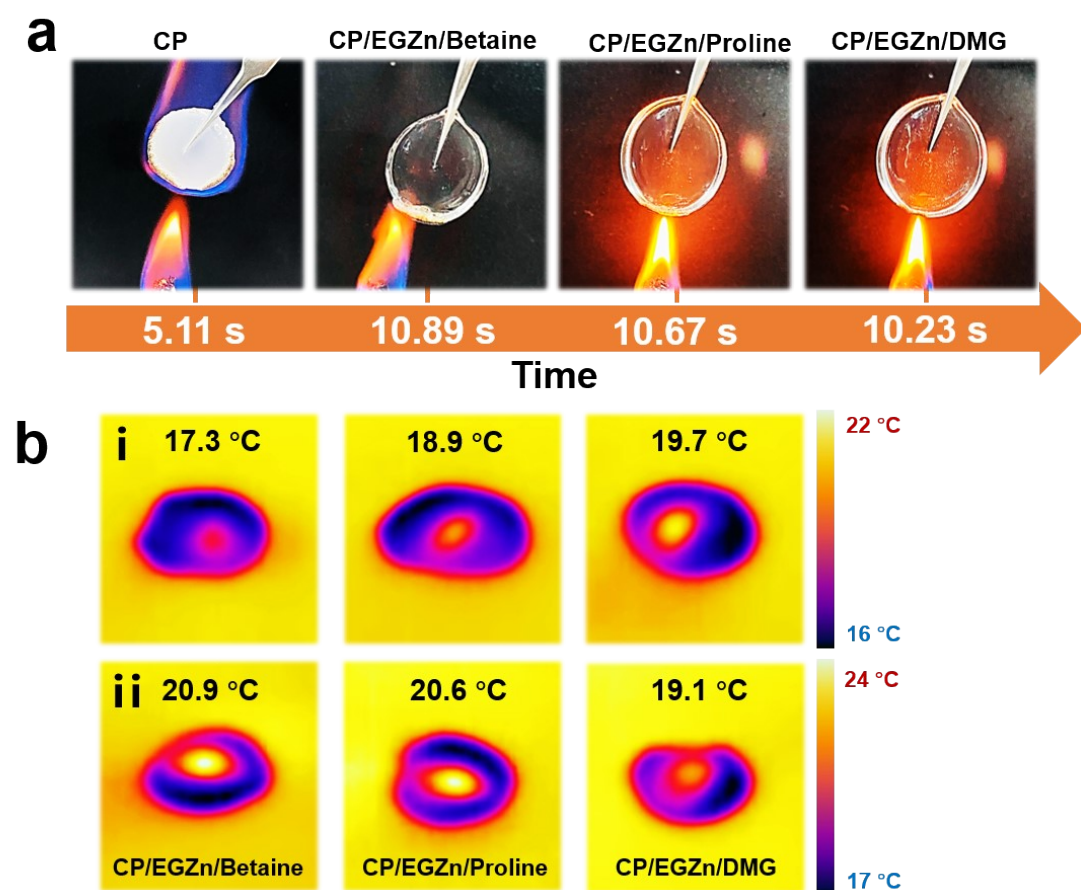


**Figure S6.** (a) Ignition tests of the CP, CP/EGZn/betaine, CP/EGZn/proline, CP/EGZn/DMG hydrogel electrolytes. (b) Infrared radiation (IR) pictures of the CP/EGZn/zwitterion hydrogel demonstrating the in-plane (i) and axial (ii) thermal-

conduction properties.

The high boiling and flash points of EG can improve the safety and reduce the risk of explosion even in the worst scenario of electrolyte leakage and thermal runaway.[4] In addition, the superb capacity of the CP/EGZn/zwitterion hydrogel with moisturizing factors to lock water is instrumental in flame retardant.



**Figure S7.** Large-scale production of the CP/EGZn/betaine hydrogel electrolyte.
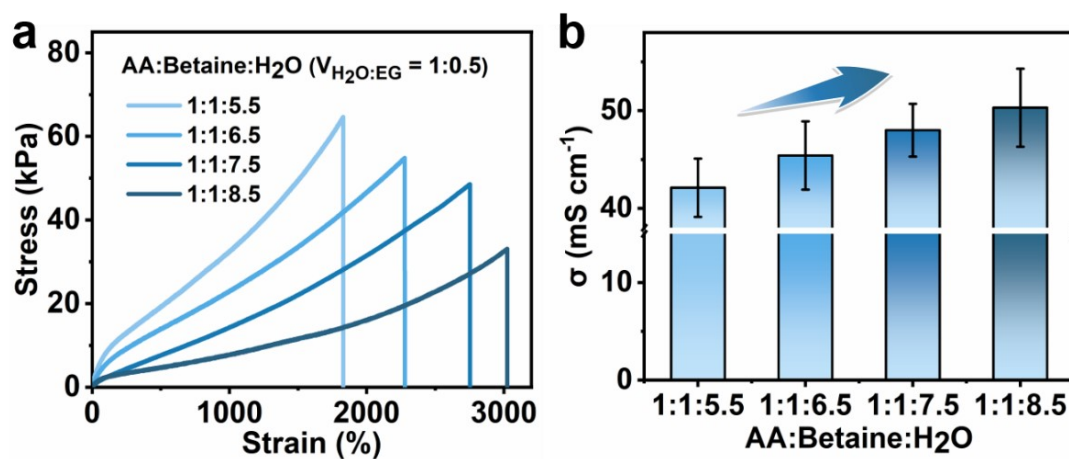


**Figure S8.** (a) Tensile stress-strain curves and (b) conductivity of the as-prepared P/EGZn/betaine hydrogels with different water contents (volume ratio, $H_2O$:EG = 1:0.5).

The P/EGZn/betaine hydrogels become much more stretchable with a decreased tensile strength as the feed molar ratio of water increases. This is reasonable because a high amount of water as a plasticizer would weaken both the PAA dimeric bonds and

betaine ionic complexes in P/EGZn/betaine hydrogels (***Nat Commun*** **2021,12, 4082**). Noticeably, an increased trend in conductivity can be observed by simply increasing the feed molar ratio of water in the as-prepared P/EGZn/betaine hydrogels, which is ascribed to the water that can improve ion transport of hydrogel electrolytes ***(Adv. Funct. Mater.* 2021, 31, 2100251;** ***Adv. Energy Mater.* 2022, 2200401;** ***Energy Storage Mater.* 2022, 48, 244–262**).
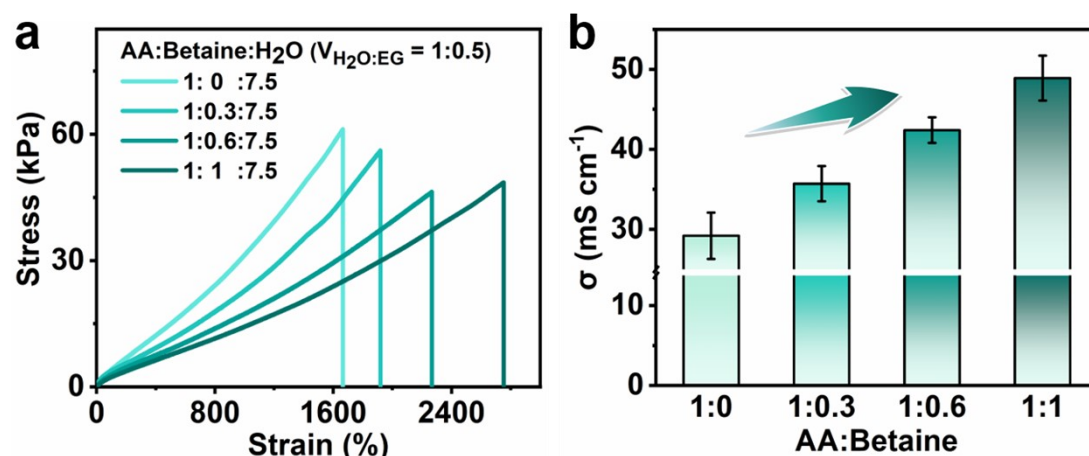


**Figure S9.** (a) Tensile stress-strain curves and (b) conductivity of the as-prepared P/ EGZn/betaine hydrogels with different molar ratios of AA and betaine (volume ratio, $H_2O$:EG = 1:0.5).

Increasing the ratio of betaine leads to more soft hydrogels, and the stretchability is largely increased, verifying the importance of dual-network design (***Nat Commun*** **2021,12, 4082**). Besides, the benefits of zwitterions as electrolyte additives for zinc ion batteries can boost target ion transport, thereby improving the conductivity of P/EGZn/betaine hydrogel electrolytes (***Nat. Mater.* 2022, 21, 228–236**).
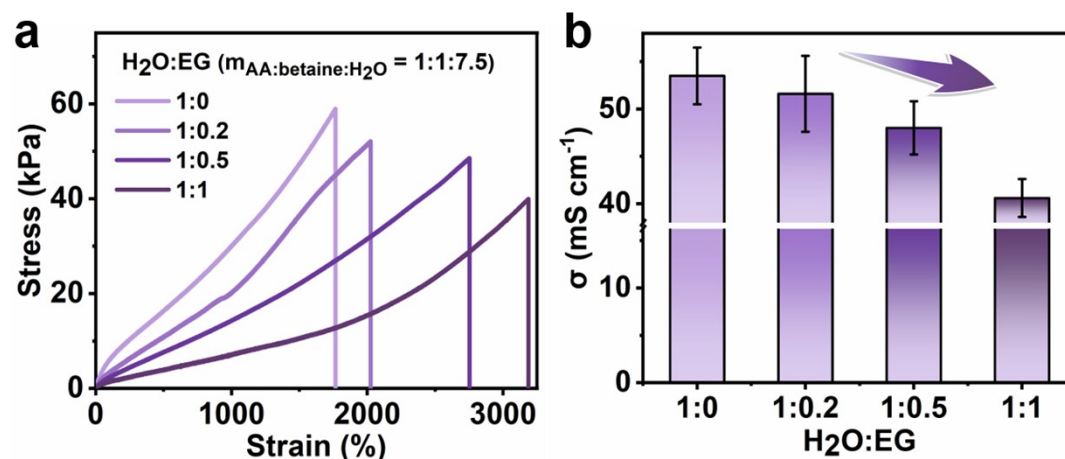


**Figure S10.** (a) Tensile stress-strain curves and (b) conductivity of the as-prepared P/

EGZn/betaine hydrogels with different volume ratios of $H_2O$ and EG (molar ratio, AA: zwitterion:$H_2O$ = 1:1:7.5).

Decreasing the amount of EG in the P/EGZn/betaine hydrogels significantly weakens the strain-stiffening effect as well as stretchability, which can be rationalized by the plasticizing behavior of EG that reduces the formation probability of H-bonds between polymer molecules and weakens the coordination bonds between polymer molecules/ $Zn^{2+}$ (***Adv. Funct. Mater. 2022, 32, 2201335***). Simultaneously, the conductivity of the P/EGZn/betaine hydrogel electrolytes decreases in the order of the increased amount of EG, ascribing to the gradually increased $Zn^{2+}$ solvation structure radii and the electrolyte viscosity (***Energy Environ. Sci., 2020,13, 4625-4665; Energy Environ. Sci., 2019,12, 706-715; Energy Environ. Sci., 2022, 15, 550-578; Energy Storage Mater. 2021, 41, 599–605; Small 2021, 17, 2103195***).
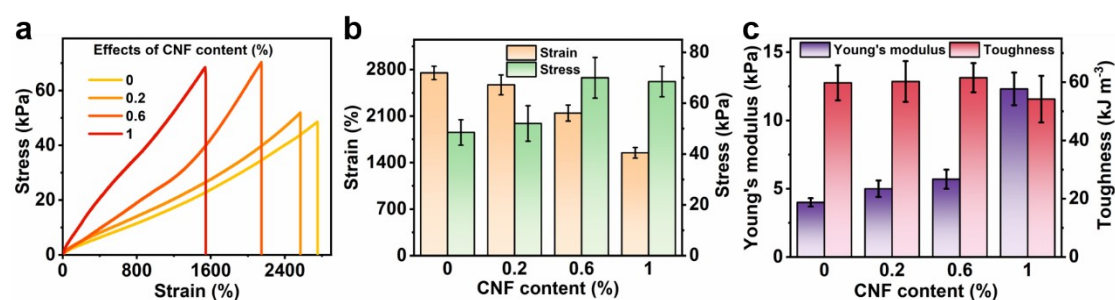


**Figure S11.** (a) Tensile stress-strain curves, (b) Maximum strain and fracture strength, and (c) Young's modulus and toughness of the CP/EGZn/betaine hydrogels with different CNF contents (0%, 0.2%, 0.6%, and 1%). Error bars indicate SD (n = 3 independent samples).
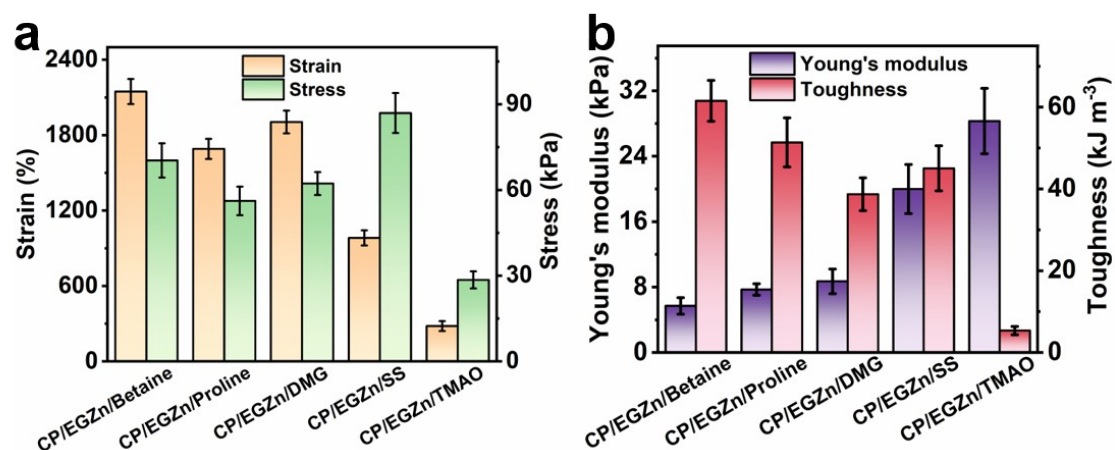


**Figure S12.** (a) Maximum strain and fracture strength and (b) Young's modulus and

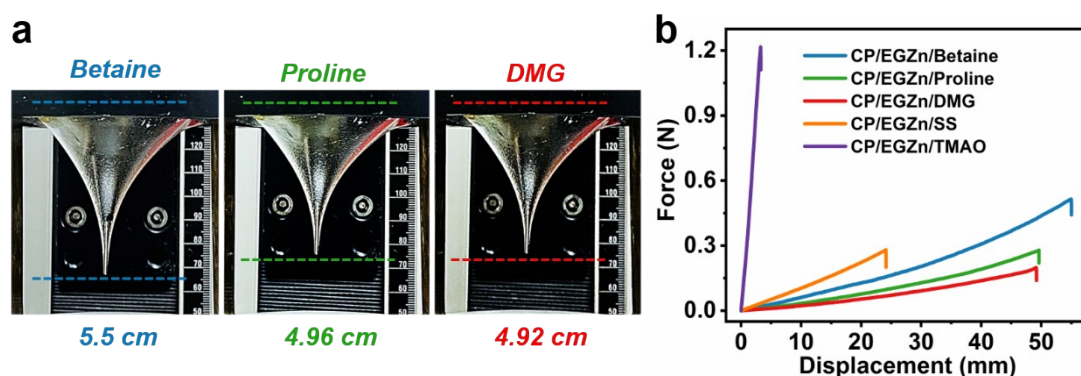toughness of the CP/EGZn/zwitterion hydrogels. Error bars indicate SD (n = 3 independent samples).



**Figure S13.** (a) Photographs showing the puncture resistance of the CP/EGZn/betaine hydrogels. (b) Puncture force-displacement curves of as-prepared CP/EGZn/ zwitterion hydrogels.

**Supplementary Note 1:**

For soft and stretchable electronics, puncture damages including hole or point defects are problematic because a small defect can induce significant stress concentration on being deformed, thus causing the whole device to break easily with function failure. To further demonstrate the ability of CP/EGZn/betaine hydrogel electrolyte to resist sharp attack that crucial for mechanical protection, puncture resistance tests are performed by puncturing the samples via a needle with a tip radius of 450 μm (**see details in the mechanical measurements**). As shown in **Figure S13**, when being pierced, the unparalleled puncture displacement and puncture energy ($\Gamma$) for the CP/ EGZn/betaine hydrogel electrolyte (1 mm in thickness) with a force as high as 0.52 N are demonstrated at 5.5 cm and 11.51 mJ, which far exceed that of the CP/EGZn/ proline hydrogel electrolyte (4.96 cm and 5.54 mJ), CP/EGZn/DMG hydrogel electrolyte (4.92 cm and 3.84 mJ), CP/EGZn/SS hydrogel electrolyte (2.41 cm and 3.17 mJ), and CP/EGZn/SS hydrogel electrolyte (0.33 cm and 1.94 mJ), indicating its exceptional mechanical robustness.
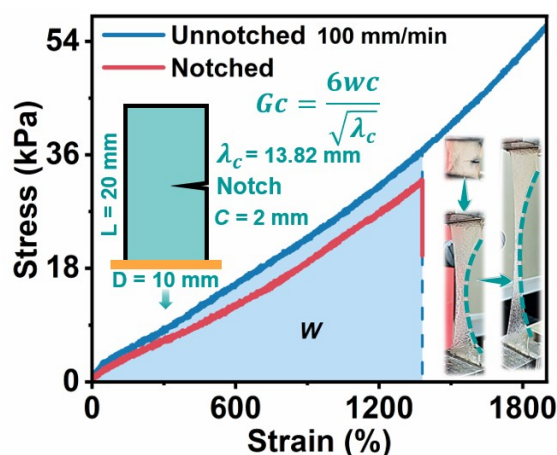
**Figure S14.** Typical stress–strain curves of the unnotched and notched CP/EGZn/betaine hydrogels.

**Supplementary Note 2:**

Similarly, the crack tolerance is a critical aspect of the CP/EGZn/betaine hydrogel electrolyte, particularly protecting them from external attacks. According to the well-established Greensmith method, fracture energy is calculated to quantitatively evaluate the crack tolerance via a single-edged notched experiment.[5] Thanks to the excellent energy dissipation capability, the pre-damaged CP/EGZn/betaine hydrogel electrolyte with a notch (width of 2 mm) exhibits superb crack tolerance, where the crack gradually widens along the longitudinal direction but hardly propagates laterally until the occurrence of specimen break at a strain and stress of 1398% and 32.1 kPa (**Figure S14**). Indeed, this high-level fracture energy of 2547 J m$^{-2}$ of the CP/EGZn/betaine hydrogel electrolyte can be ascribed to the dynamic rupture and reformation of the reversible H-bonds and coordination bonds, and the stress concentration at the crack tip is effectively transferred to the neighboring polymer chains and prohibits the lateral crack propagation.
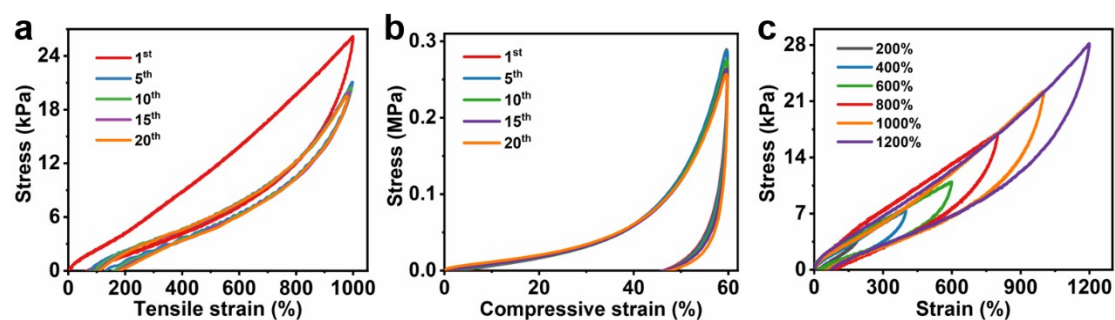


**Figure S15.** (a) Consecutive loading-unloading cycle curves at a constant tensile strain of 1000% and (b) a constant compressive strain of 60%without resting between

each cycle of the CP/EGZn/betaine hydrogel. (c) Tensile stress-strain curves at different strains of the CP/EGZn/betaine hydrogel. The area of the stress-strain curves increases with the increase in the tensile strain, indicating that the CP/EGZn/betaine hydrogel can dissipate more energies to withstand the strain change without mechanical damage.
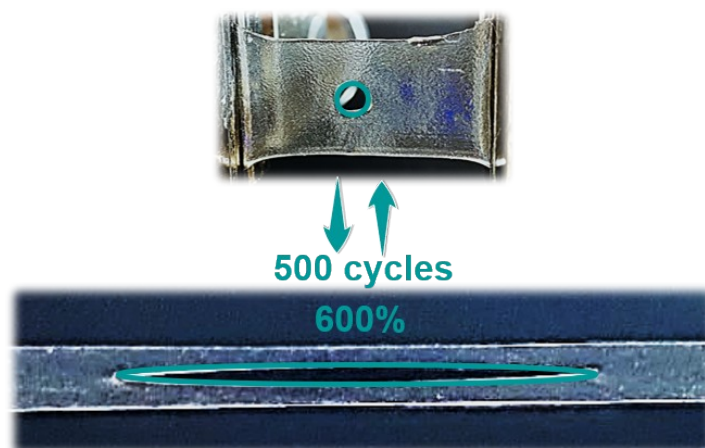


**Figure S16.** Digital snapshot of the CP/EGZn/betaine hydrogel with a hole after 500 continuous stretching cycles at a constant strain of 600%.
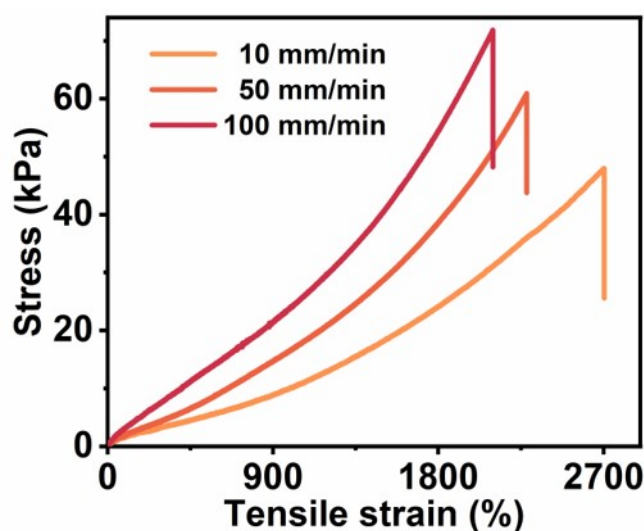


**Figure S17.** Tensile stress-strain curves of the CP/EGZn/betaine hydrogels at different strain rates.

To correlate the mechanical properties of the CP/EGZn/betaine hydrogels to the H-bond network dynamics, we examine mechanical testing at different stretching rates (10-100 mm min$^{-1}$ in **Figure S17**). The CP/EGZn/betaine hydrogels strained quickly

(100 mm min$^{-1}$), demonstrating the highest stress at break and the highest modulus in each regime. It is well known that on time scales shorter than the association time of the reversible bonds, the dynamic crosslinks act as a strong network and the material is elastic.[6] This occurs because the relative time scale of deformation is shorter than the lifetime of the H-bonds, thus the H-bonds act as strong crosslinks and the elastic character of the material dominate. Alternatively, when samples are strained slowly, dynamic rearrangement of the H-bonds (transient crosslinks) can occur which enhances the viscous characteristics of the material. In this context, when strained at 10 mm min$^{-1}$, the CP/EGZn/betaine hydrogels exhibit higher strains at break and a slower accumulation of stress than materials that are stretched more quickly.
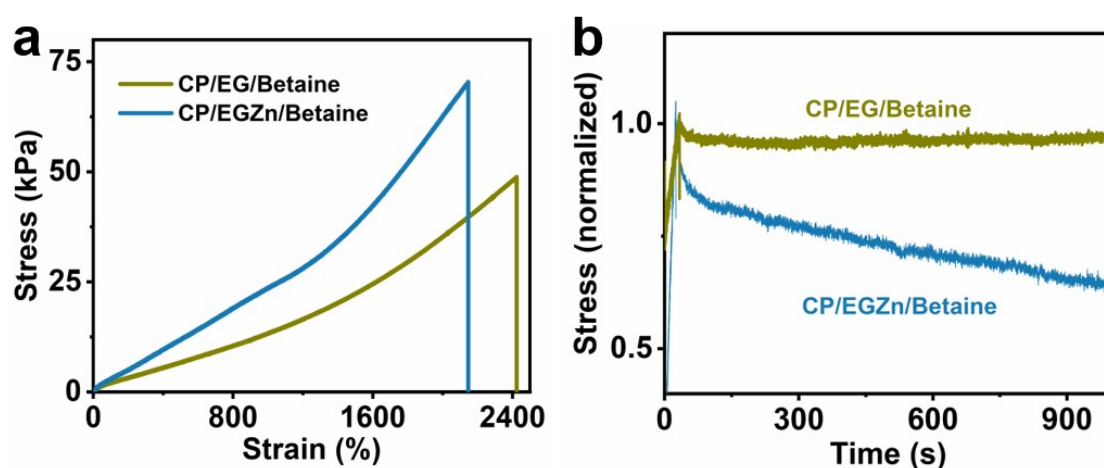


**Figure S18.** (a) Tensile stress-strain curves of the CP/EG/betaine and CP/EGZn/ betaine hydrogels. (b) The stress relaxation curves of the CP/EG/betaine and CP/EGZn/ betaine hydrogels stretched at 300% strain for 1000 s.

The typical strain–stress curves in **Figure S18a** unravel that the incorporation of 2 M ZnSO$_4$ severely toughens CP/EG/betaine, ascribed to the coordination bonds between Zn$^{2+}$ and the carboxyl groups contained in the CP/betaine complex. As proved by the stress relaxation test in **Figure S18b**, the release of applied force of the CP/EGZn/ betaine hydrogels is apparently higher than that of the CP/EG/betaine hydrogels due to the incorporation of Zn$^{2+}$, exhibiting the efficient energy dissipation of the coordination bonds.

**Supplementary Note 3**

(1) The interpenetrating entanglement between covalently crosslinked PAA networks and supramolecular zwitterion chains via reversible H-bonds and coordination bonds (**Figure S3,S4,S17,S18**), along with the CNF reinforcement, impart exceptional mechanical robustness, allowing for resistance to mechanical impact.

(2) SZHEs feature zwitterionic groups for constructing ion migration channels (**Figure 7c**), which largely facilitates $Zn^{2+}$ transport for the top-ranking ionic conductivity and transfer number.

(3) Enabled by the incorporation of a hydrated $ZnSO_4$ salt with an EG and zwitterions with moisturizing factors, the SZHEs exhibit moisture-preserving, anti-freezing, and anti-heating advantages, affording mechano-interfacial robustness and steady transport ions even in extreme conditions (**Figure 5**).

**Supplementary Note 4**

More intriguingly, the reversible H-bonds between the hydroxyl and carboxyl groups as well as the coordination bonds (**Figure S3,S4,S17,S18**) between $Zn^{2+}$ and the carboxyl groups contained in the zwitterion/CP complex endow the SZHEs with reliable self-healing properties, which construct the dynamically self-adaptive interface with a superb capability to in-situ repair the cycling-induced cracks.
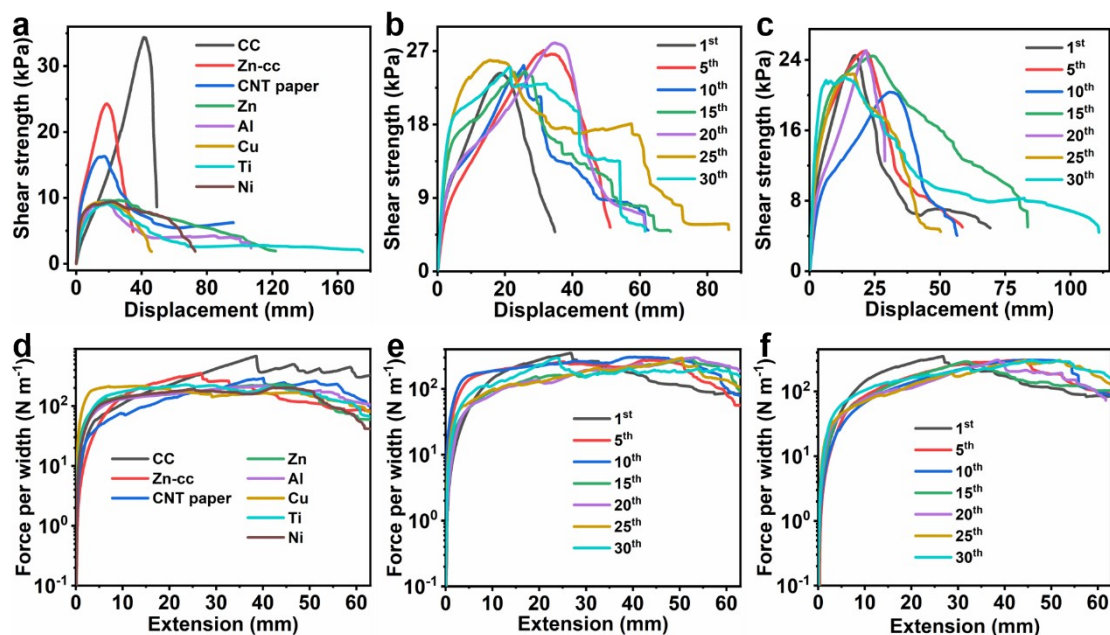
**Figure S19.** a) Lap shear curves of the CP/EGZn/betaine hydrogel electrolytes on diverse electrodes including carbon electrodes (CC and CNT paper) and metals (Zn, Al, Cu, Ti, and Ni). Lap shear curves of the CP/EGZn/betaine hydrogel electrolytes to Zn-cc at different b) peeling-off cycles and c) storage days. d) 180° peeling curves of the CP/EGZn/betaine hydrogel electrolytes on diverse electrodes. 180° peeling curves of the CP/EGZn/betaine hydrogel electrolytes to Zn-cc at different e) peeling-off cycles and f) storage days.
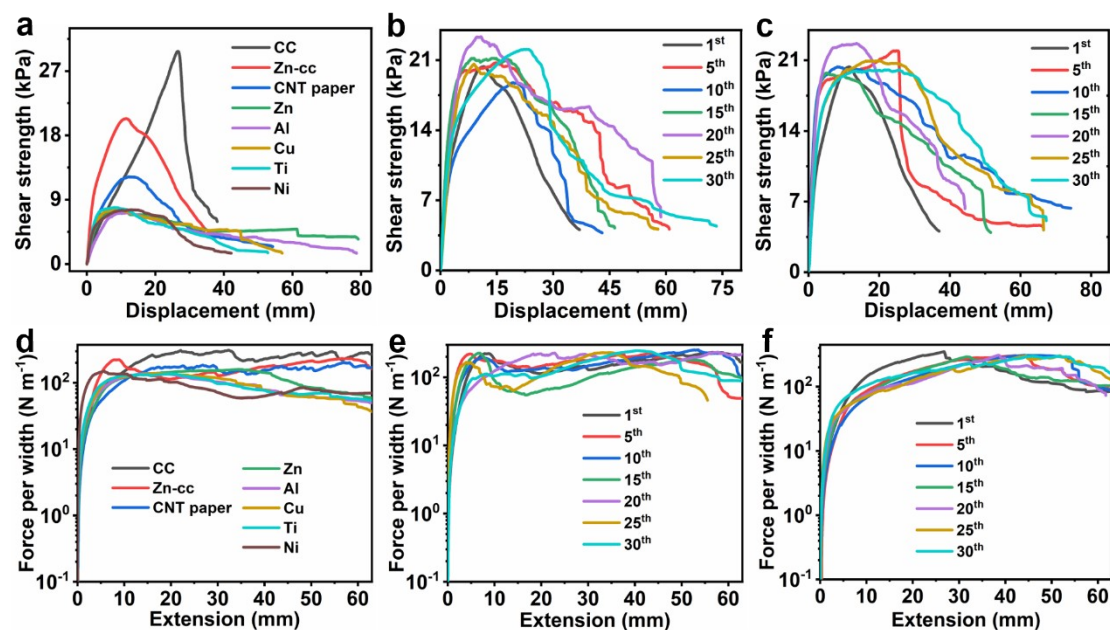


**Figure S20.** a) Lap shear curves of the CP/EGZn/proline hydrogel electrolytes on diverse electrodes including carbon electrodes (CC and CNT paper) and metals (Zn,

Al, Cu, Ti, and Ni). Lap shear curves of the CP/EGZn/proline hydrogel electrolytes to Zn-cc at different b) peeling-off cycles and c) storage days. d) 180° peeling curves of the CP/EGZn/proline hydrogel electrolytes on diverse electrodes. 180° peeling curves of the CP/EGZn/proline hydrogel electrolytes to Zn-cc at different e) peeling-off cycles and f) storage days.
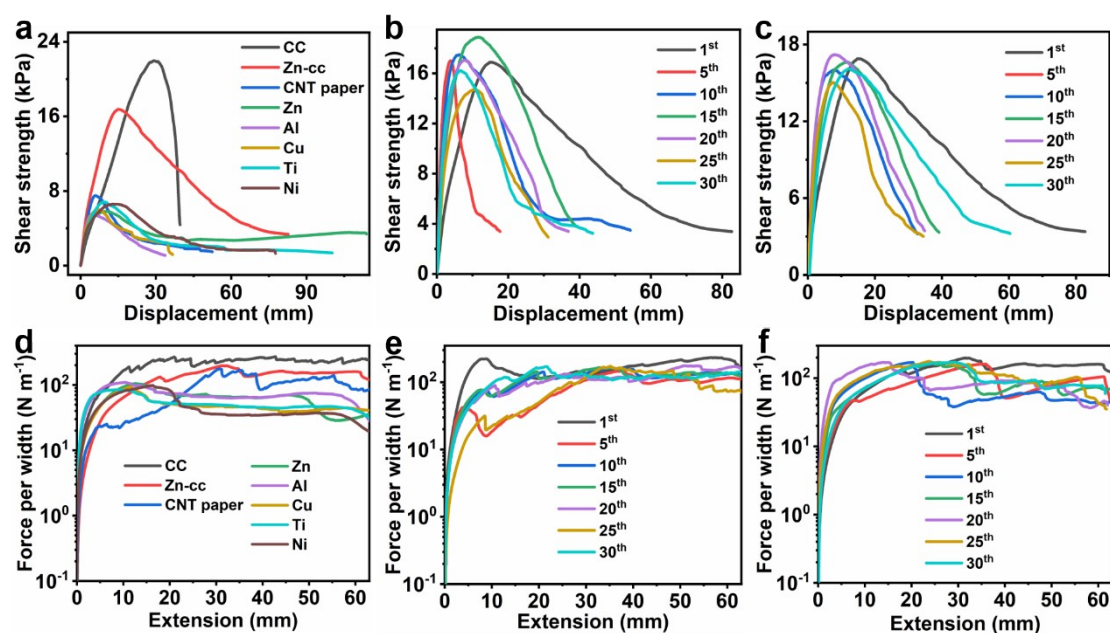


**Figure S21.** a) Lap shear curves of the CP/EGZn/DMG hydrogel electrolytes on diverse electrodes including carbon electrodes (CC and CNT paper) and metals (Zn, Al, Cu, Ti, and Ni). Lap shear curves of the CP/EGZn/DMG hydrogel electrolytes to Zn-cc at different b) peeling-off cycles and c) storage days. d) 180° peeling curves of the CP/EGZn/DMG hydrogel electrolytes on diverse electrodes. 180° peeling curves of the CP/EGZn/DMG hydrogel electrolytes to Zn-cc at different e) peeling-off cycles and f) storage days.
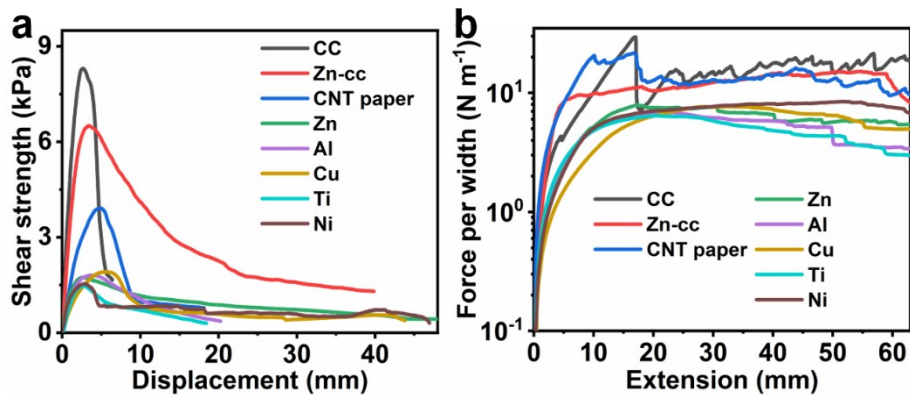
**Figure S22.** a) Lap shear curves and b) 180° peeling curves of the CP/EGZn/DMG hydrogel electrolytes on diverse electrodes including carbon electrodes (CC and CNT paper) and metals (Zn, Al, Cu, Ti, and Ni).
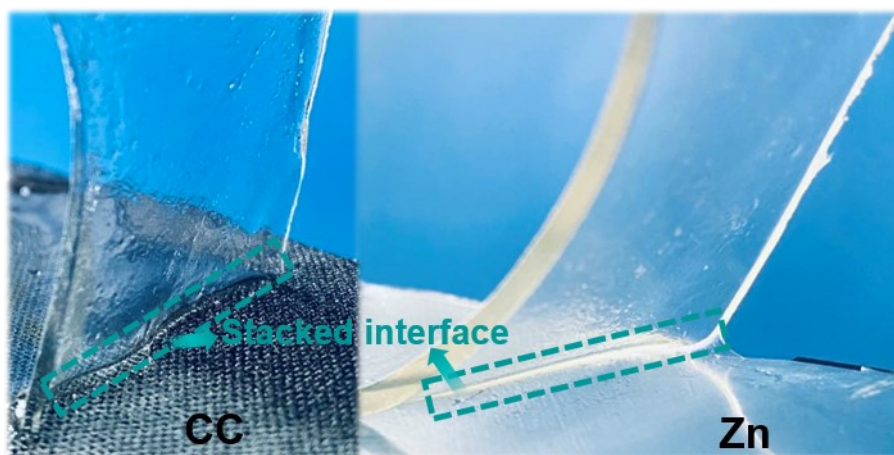


**Figure S23.** Photographs showing peel off of the CP/EGZn hydrogel electrolyte from the carbon cloth and Zn sheet for stacked interfaces.



**Figure S24.** Metre-scale ZIC tapes made of the CP/EGZn/betaine hydrogel electrolytes that sandwiched between Zn sheet and cc.
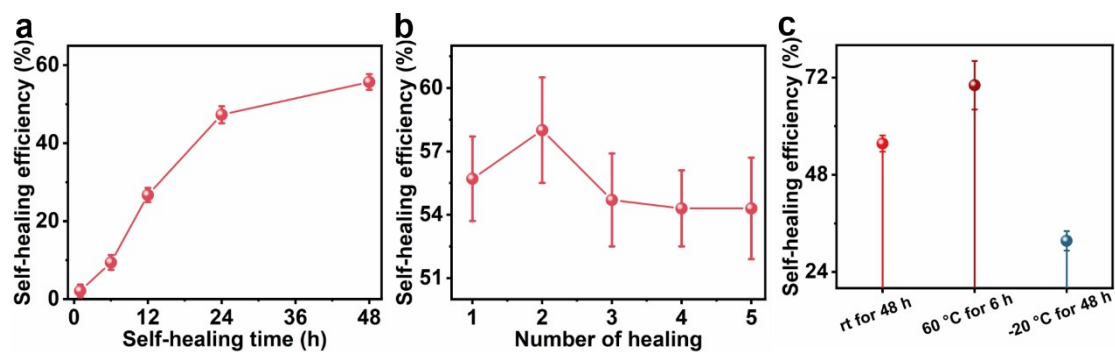
**Figure S25.** Plots of self-healing efficiency (%) of the CP/EGZn/betaine hydrogel electrolyte versus a) repair time, b) healing cycles, and c) healing conditions. Error bars indicate SD.
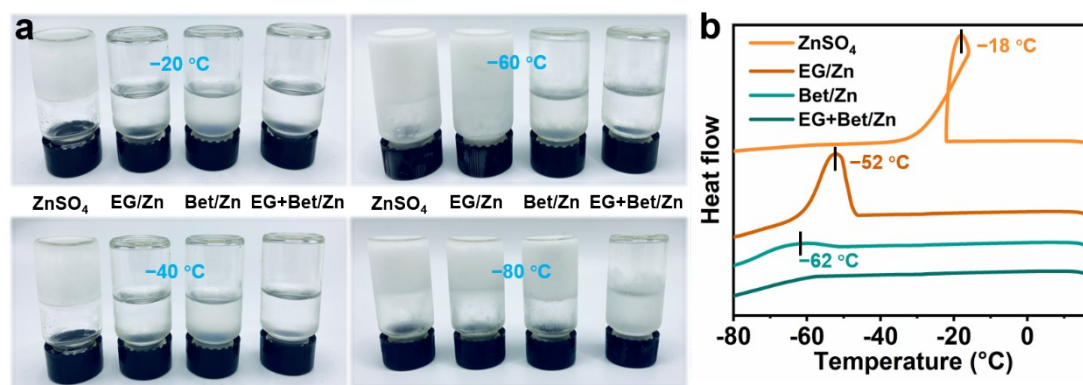


**Figure S26.** (a) Optical photographs of $ZnSO_4$ (Zn), EG/Zn, Betaine (Bet)/Zn, and EG+Bet/EG electrolytes at −20, −40,−60, and −80 °C. (b) DSC test from 20 to −80 °C at a freezing rate of 5 °C min$^{-1}$.

It is found that $H_2O$ molecules in $ZnSO_4$ electrolyte form a self-associated periodic crystal structure (ice) through H-bonds at −18 °C, which means that $Zn^{2+}$ is confined in the crystal lattice and cannot move. In contrast, the glass–liquid transition process of Bet/$ZnSO_4$ electrolyte occurs −62 °C, whereas the freezing point of EG/$ZnSO_4$ electrolyte is only −52 °C. Therefore, betaine is more important for the anti-freezing performance of the hydrogel than that of EG.
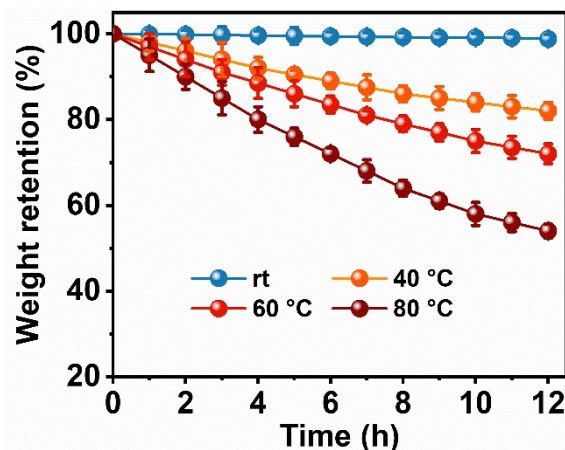
**Figure S27.** Weight retention ratio of the CP/EGZn/betaine hydrogel electrolyte versus time at different temperatures.
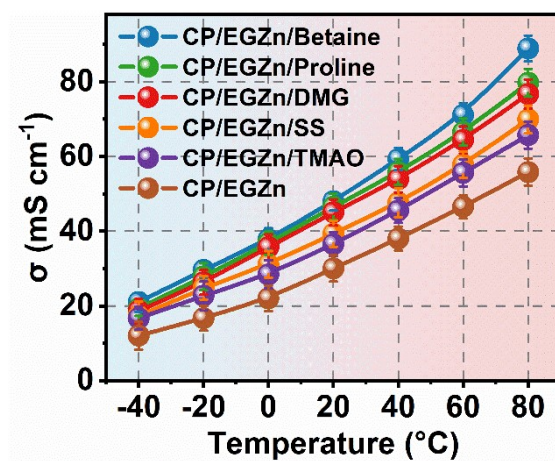


**Figure S28.** Ionic conductivity of the CP/EGZn/zwitterion and the CP/EGZn hydrogel electrolytes over a wide temperature range.
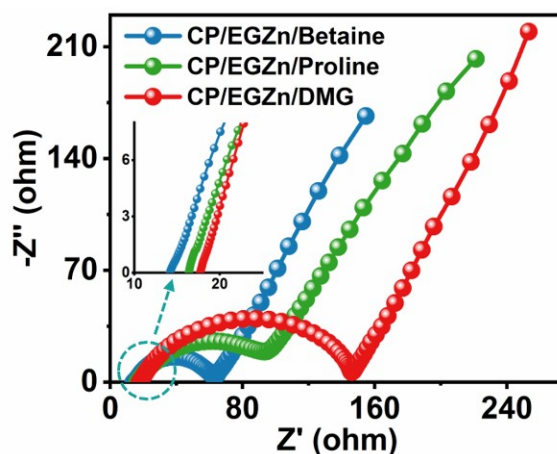


**Figure S29.** (g) Electrochemical impedance spectroscopy (EIS) of ZICs with the CP/EGZn/betaine, CP/EGZn/Proline, and CP/EGZn/DMG hydrogel electrolytes.

**Supplementary Note 5**

Small dipole molecules (small molecules containing a dipole; Betaine (Bet) with amides and EG with hydroxyl groups) with strong Lewis alkalinity can deplete the water molecules in the solvation-sheath structure of cations without sacrificing the superior ion conductivity of aqueous electrolytes, which may be caused by **the cations in the EG-containing electrolyte diffuse through jump mechanism and the cations in the Bet-containing electrolytes diffuse through solvation sheath transport mechanism** (*Adv. Mater.* **2022**, *34*, **2106180**). The two types of ion-transport mechanism can be described as following: (1) The solvation-sheath structure of $Zn^{2+}$ underwent a series of variations from $Zn[H_2O]_2[EG]_2^{2+}$ to $Zn[H_2O]_2[EG]_3^{2+}$ to $Zn[H_2O]_2[EG]_2^{2+}$ during the transport process, which belongs to a kind of jump mechanism. (2) The $Zn^{2+}$ in Bet electrolyte are transported in the form of solvation-sheath structure ($Zn[H_2O]_3[Bet]_3^{2+}$) during the whole diffusion process, indicative of the strong interactions between $Zn^{2+}$, Bet, and $H_2O$. This special ion-transport mechanism provides the explanation for that the betaine and EG electrolyte has a good ion conductivity and high $Zn^{2+}$ transference number.
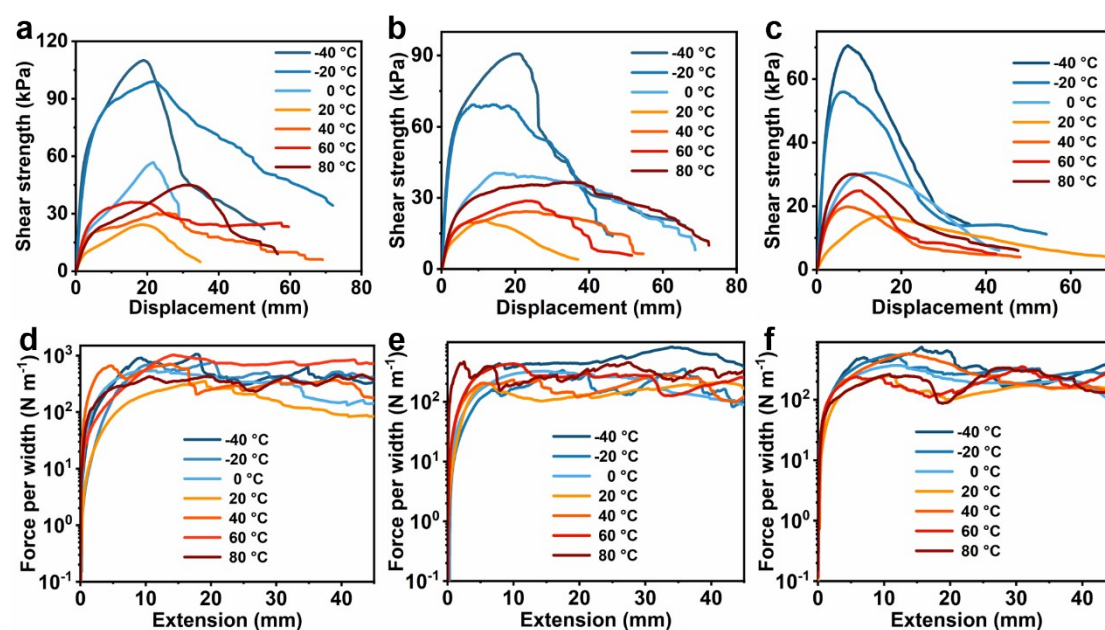


**Figure S30.** Lap shear and 180° peeling curves of a,d) the CP/EGZn/betaine, b,e) the CP/EGZn/proline, and c,f) the CP/EGZn/DMG hydrogel electrolytes on Zn-cc at different temperatures, respectively.
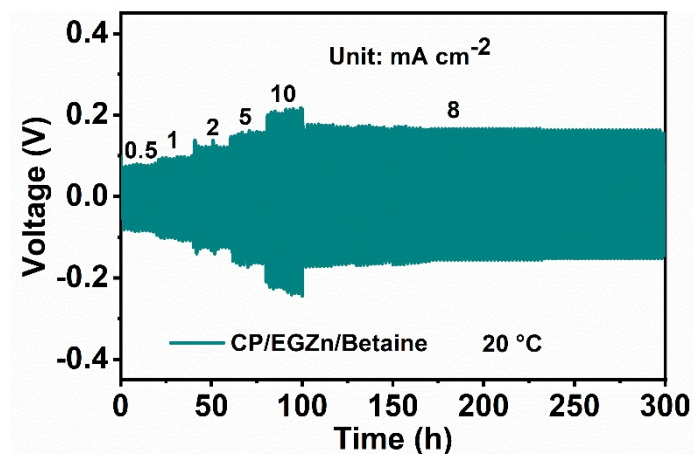
**Figure S31.** The cycling performance of the Zn/Zn symmetrical cell with CP/EGZn/ betaine at various current densities.
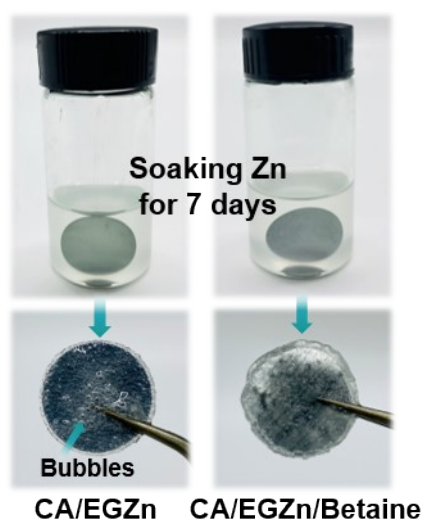


**Figure S32. The stability of Zn in CA/EGZn and CA/EGZn/Betaine electrolytes (A representing AA solution).** Optical photographs of the Zn soaked in (a) CA/EGZn electrolyte and (b) CA/EGZn/Betaine electrolyte for 7 days.

In the CA/EGZn electrolyte, the Zn surface gradually changes from the bright metallic color into dark gray with lots of bubbles, revealing the progressively aggravated corrosion reactions. In sharp contrast, Zn metal surface maintains a light gray color with betaine additive, indicating that side effects are greatly suppressed (***Adv. Mater.* 2022, 34, 2206754**).
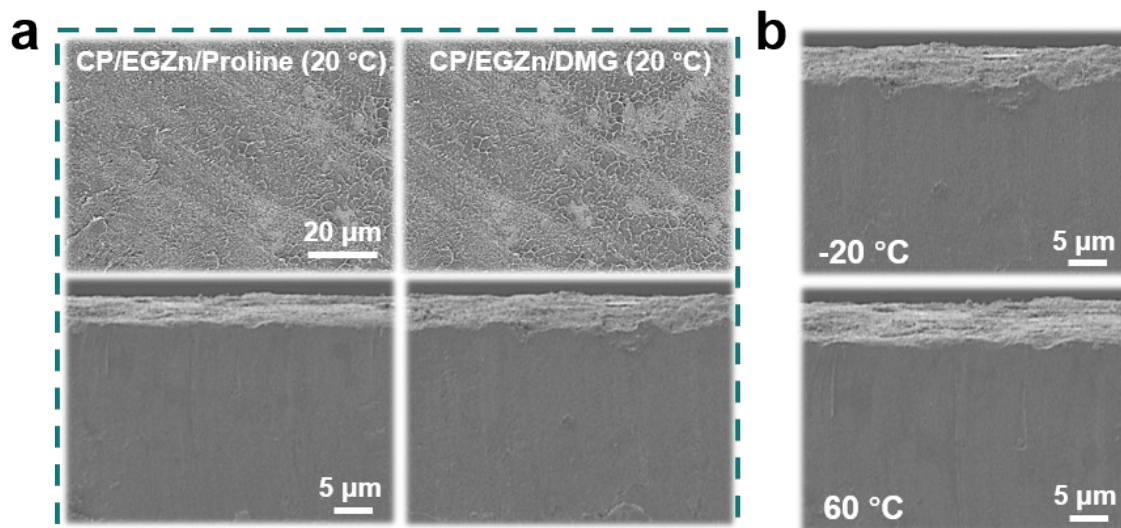
**Figure S33.** a) Surface and cross-sectional SEM images of the Zn foils in Zn/Zn cells with CP/EGZn/proline and CP/EGZn/DMG hydrogel electrolytes after 50 h. b) Zn anodes after stripping–plating for 50 h with CP/EGZn/betaine hydrogel electrolytes at −20 and 60 °C, respectively.
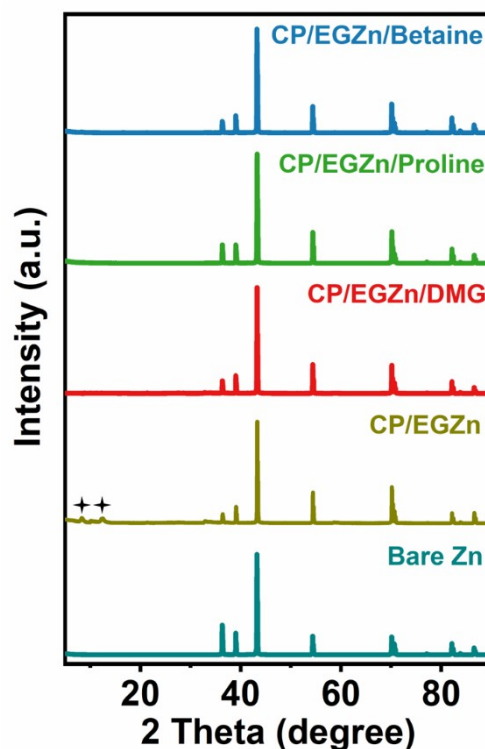


**Figure S34.** XRD patterns of bare Zn and the Zn anodes in Zn/Zn symmetrical cells with CP/EGZn, CP/EGZn/DMG, CP/EGZn/proline, and CP/EGZn/betaine hydrogel electrolytes after 50 h cycling at 1 mA cm$^{-2}$.

.
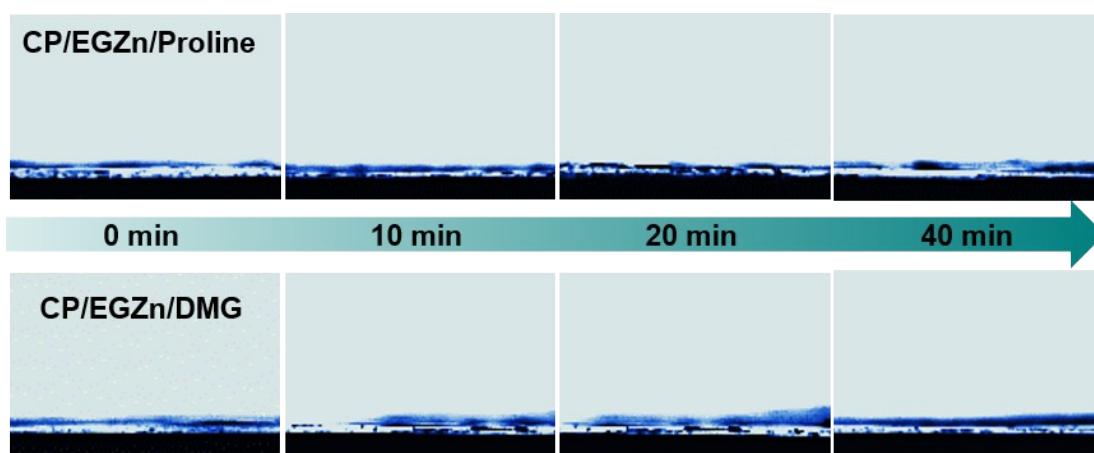
**Figure S35.** Optical microscopy cross-section images of Zn anodes with CP/EGZn/ proline and CP/EGZn/DMG hydrogel electrolytes at 5 mA cm$^{-2}$ for 40 min.
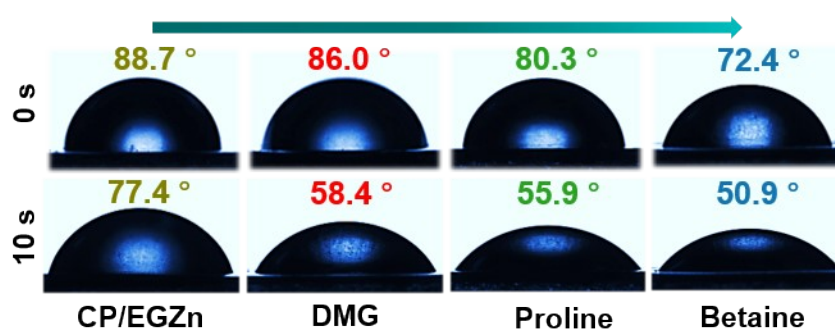


**Figure S36.** The photos showing the evolutions of the contact angles between the CP/ EGZn, CP/EGZn/DMG, CP/EGZn/proline, and CP/EGZn/betaine electrolytes and Zn anodes.
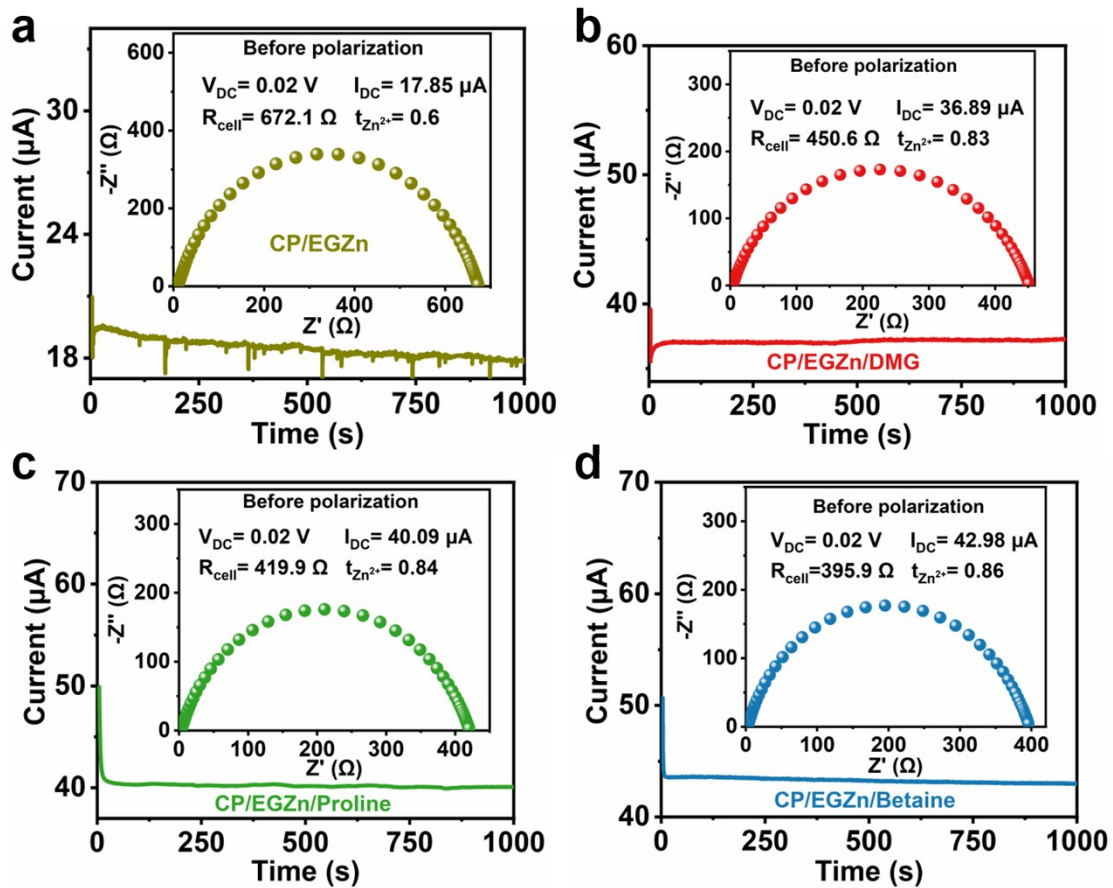
**Figure S37.** $Zn^{2+}$ transference number characterization of the a) CP/EGZn, b) CP/EGZn/DMG, c) CP/EGZn/proline, and d) CP/EGZn/betaine electrolytes with the applied voltage of 20 mV. Inset of the impedance curve before polarization.
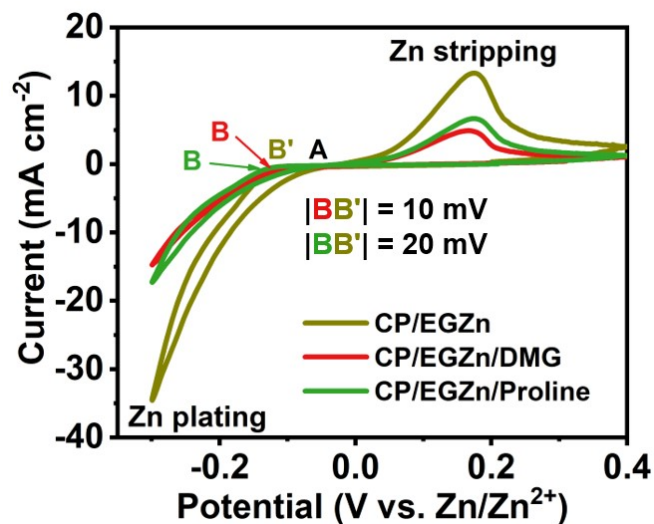


**Figure S38.** CV curves of Zn‖Ti cells tested in CP/EGZn, CP/EGZn/DMG, and CP/EGZn/proline hydrogel electrolytes at a scan rate of 1 mV s$^{-1}$.
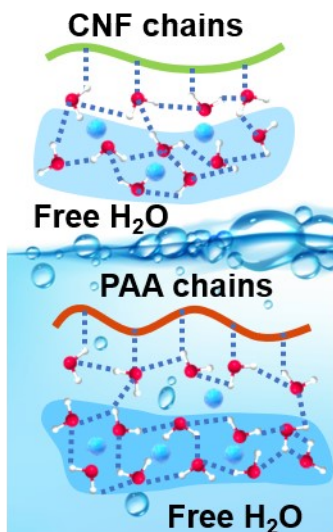
**Figure S39.** Mechanisms of the $H_2O$ and $Zn^{2+}$ ions captured by the CNF and PAA
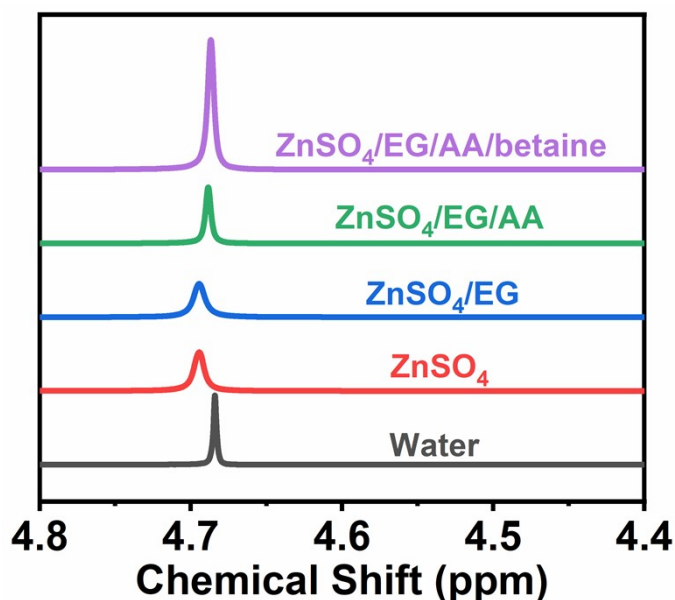


**Figure S40.** $^1H$ NMR spectra of water molecules in different solutions of pure water, $ZnSO_4$, $ZnSO_4/EG$, $ZnSO_4/EG/AA$, and $ZnSO_4/EG/AA/betaine$.

Notably, the $^1H$ peaks all shift to the higher field with the presence of $ZnSO_4$, $ZnSO_4/EG$, $ZnSO_4/EG/AA$, and $ZnSO_4/EG/AA/betaine$, substantiating that the H-bond of water molecules is weakened in these solutions. In particular, the $^1H$ peaks of $ZnSO_4/EG/AA/betaine$ show an incremental increase in intensity after introducing betaine, which may be ascribed to the strong interactions between betaine and $H_2O$, containing H-bonds (N…H-O and O…H-O).
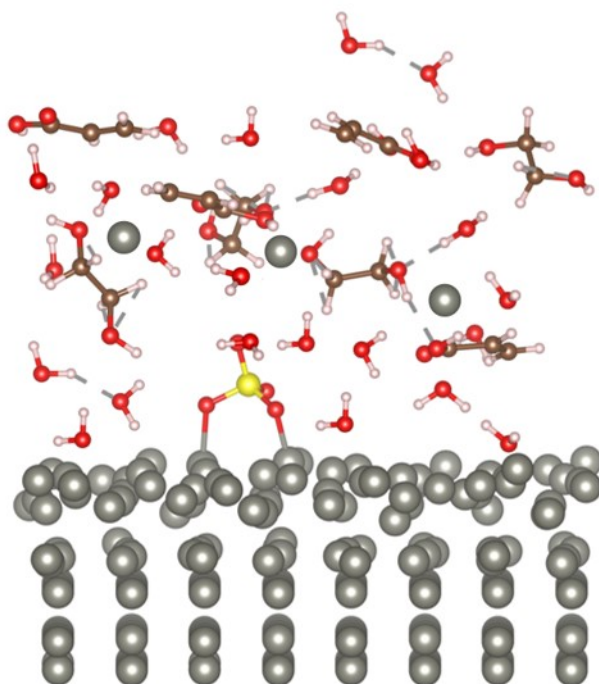
**Figure S41.** The snapshot of the Zn$^{2+}$-solvation structure on the surface of the CP/ EGZn @Zn electrode obtained from the AIMD simulations.
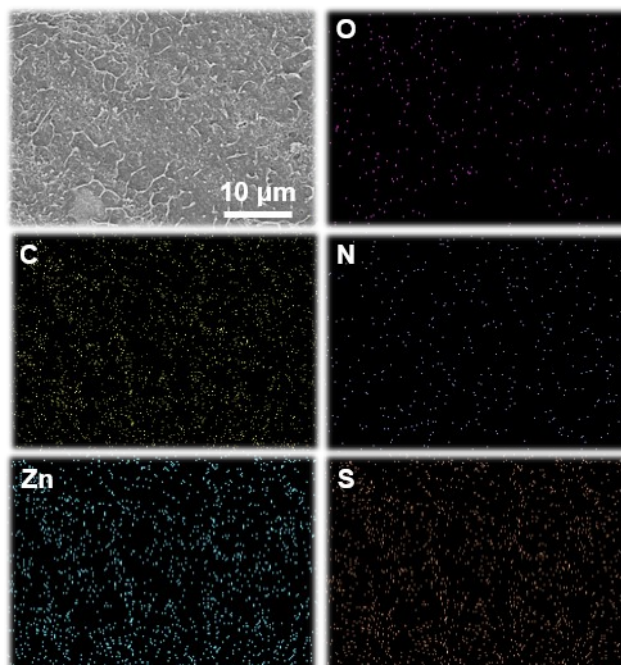


**Figure S42.** SEM image and EDS element maps of the anode after 50 h cycling.

In the SEM image (**Figure S42**), the zinc anode after 50 h cycling in the CP/EGZn/ betaine hydrogel layer exhibits a smooth surface and dense and dendrite-free morphology without break and degradation. Based on the EDS results, in addition to Zn, the hydrogel layer is composed of mainly C, N, and O, suggesting its zwitterion structure with a quaternary ammonium containing $Zn^{2+}$, which verifies the existence of a uniform quasi-solid-electrolyte-interphase layer with favorable self-healing capacity.

**Supplementary Note 6:**

1. **Mechanical Performance:** betaine, proline, and DMG better than SS and TMAO

The slight drop of the strength and stretchability of CP/EGZn/zwitterion hydrogels is in order of betaine, DMG, and proline (**Figure S12a**), which may result from the reduced zwitterion-PAA interactions in the case of tertiary and secondary amines with a lower electropositivity (***Nat Commun* 2021, 12, 4082**). The other two CP/EGZn/ zwitterion hydrogels show a sharp drop of stretchability in the order of SS and TMAO. This order is in full accordance with the increment of the acid dissociation constants ($pK_a$) of zwitterions, which may be caused by the increased deprotonation degree of PAA (**Figure S1**), resulting in weaker COOH dimeric H-bonds (***Nat Commun* 2021, 12, 4082**).

The initial moduli of the five CP/EGZn/zwitterion hydrogels increase in the order of betaine, proline, DMG, SS, and TMAO (**Figure S12b**), mainly arising from the increasing relative amount of H-bonded PAA (corresponding to the formation of more H-bonded crosslinks) as elucidated by attenuated total reflection-Fourier transform infrared (ATR-FTIR) spectral comparison (**Figure S4b**).

2. **Interfacial Compatibility:** betaine, proline, and DMG better than SS and TMAO
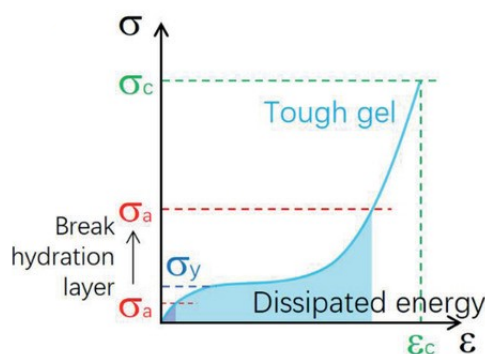


An illustration of the general mechanical principle for a strong adhesive. The blue curve represents the bulk tensile stress–strain curve of soft, but tough, material with yielding stress ($\sigma_y$), fracture stress ($\sigma_c$), and fracture strain ($\varepsilon_c$). The red dashed lines

represent the debonding stress ($\sigma_a$) of the adhesive interface. A strong but reversible adhesive requires a large $\sigma_c$ and $\varepsilon_c$ in bulk and a large $\sigma_a$ at the interface with $\sigma_y \ll \sigma_a < \sigma_c$, allowing for significant energy dissipation without cohesive failure. For hydrogel adhesives, while large $\sigma_c$ and $\varepsilon_c$ can be obtained by dynamic bonds, achieving a large $\sigma_a$ in water is challenging due to the hydration of interfaces underwater (**Adv. Funct. Mater. 2021, 31, 2009334**).

Strong hydrogel adhesion on substrates depends on both the interfacial adhesion and the cohesion of hydrogels (**Adv. Sci. 2022, 9, 2203890; J. Mater. Chem. B, 2022,10, 757-764**), namely, a repeatable and robust adhesion requires both a strong noncovalent interaction at the interface and a high toughness of the bulk material (**Adv. Funct. Mater. 2021, 31, 2009334**). The almost identical tensile curves of the three CP/EGZn/zwitterion hydrogels (betaine, proline, and DMG) with a high toughness is in full accordance with the previously reported bulk tensile stress–strain curve (**Figure 2a,S12b**), indicative of a strong adhesive. Notably, the adhesion strength and adhesion energy of betaine are greater that of proline and DMG (**Figure 3a,b**), which may be which may result from the reduced electrostatic repulsion with metal ions in the case of tertiary amines with a lower electropositivity (**Nat Commun 2021, 12, 4082**). In contrast, a sharp drop in adhesion strength and adhesion energy is obtained for the other two CP/EGZn /zwitterion hydrogels (SS and TMAO), which may be because they are too rigid (high modulus) to tightly attach to substrates (**Figure 2a,S12b and Figure 3a,b**).

On the other hand, the ionic conductivity of the CP/EGZn/zwitterion hydrogels increases in the order of TMAO, SS, DMG, proline, and betaine (**Figure S28**), which coincides with the increment of the interfacial adhesion of the CP/EGZn/zwitterion hydrogels (**Figure 3a,b**). Additinally, charge transfer resistance ($R_{ct}$) signifies the efficiency of electrons shifting across the electrode/electrolyte interface. According to EIS result, the $R_{ct}$ of the CP/EGZn/betaine hydrogel electrolytes is 13.7 $\Omega$, which is lower than 16.1 $\Omega$ and 17.6 $\Omega$ for the CP/EGZn/ proline and DMG hydrogel electrolytes, respectively (**Figure S29**), indicative of the higher charge transfer of CP/ EGZn/betaine hydrogel electrolytes with a robust interface. This may be attributed to two aspects: (1) strong interfacial adhesion, (2) a low p$K_a$ is prone to deprotonate, which thereby promoting $ZnSO_4$ dissociation and reducing $R_{ct}$.

3. **Electrochemical performance:** betaine better than proline and DMG

**H₂O-poor interface:** According to steric effect, the three methyl groups connected on betaine nitrogen induce a greater the steric hindrance than that of

proline and DMG, which are prone to repel water molecules in the solvated shell of hydrated $Zn^{2+}$, namely, hydrophobic trimethyl ammonium ($-N^+[CH_3]_3$) group. It is found that the zwitterionic molecules can be directionally adsorbed to the Zn anode surface under the applied electric field, forming strings of zwitterionic molecules that extract water out from the electrode. More zwitterionic molecules further aggregate at the outer end of the strings through intermolecular electrostatic interactions, forming a waterproof layer that successfully expels water from the Zn anode surface. Notably, the self-aggregation of zwitterionic additives in the hydrogel electrolytes successfully minimizes the influence on ion transport (***Adv. Funct. Mater. 2022, 32, 2207140***). On the other hand, betaine can preferentially adsorb on the zinc surface via a strong chemical adsorption (COO-Zn). Such a strong chemical adsorption introduces a water-poor electrical double layer (EDL), which can effectively inhibit the competitive adsorption of $H_2O$ and its subsequent induced side reactions (***Adv. Mater. 2022, 35, 2208237***; ***ACS Nano 2023, 17, 1, 552–560***).

**Solvation effect of water:** The more H combined on N induces the more chances of hydrogen bonding between ammonium positive ions and water, that is, the greater the degree of solvation of positive ions, which may lead to more water molecules into the solvated shell of hydrated $Zn^{2+}$ and cause side effects (e.g., $H_2$ evolution), thereby suffering from short cycle life of cell (***Adv. Mater. 2022, 34, 2206754***).

Therefore, the symmetrical Zn cells with CP/EGZn/betaine hydrogel electrolytes perform much better in cycle life than that of proline and DMG (**Figure 6a**).


**Supplementary Note 7**

**$H_2O$-poor environment:**

1. **The zwitterionic molecules can be directionally adsorbed to the negative electrode's surface under the applied electric field, forming strings of zwitterionic molecules that extract water out from the electrode. More zwitterionic molecules further aggregate at the outer end of the strings through intermolecular electrostatic interactions, forming a waterproof layer that successfully expels water from the electrode's surface.** As a typical example, betaine ($C_5H_{11}NO_2$), has a negatively charged, hydrophilic carboxyl (-$COO^-$) group on one end, and a positively charged but hydrophobic trimethyl ammonium ($-N^+[CH_3]_3$) group on the other end of the same monomeric unit. Considering the unique zwitterionic nature of betaine additive, we expect that, as

the electrode is negatively polarized, the hydrophobic positively charged $-N^+[CH_3]_3$ groups of betaine would move toward the electrode surface due to the strong counterion–electrode coulombic interactions, while the water molecules could be expulsed from the electrode surface since they favor the hydrophilic negatively charged -COO$^-$ groups. Moreover, driven by the intermolecular electrostatic interaction, more betaine aggregations would continuously connect to the ones preferentially adsorbed on the electrode surface at another end with hydrophilic negatively charged -COO$^-$ group (Meanwhile, the self-aggregation of zwitterionic additives in the bulk liquid successfully minimizes the influence on ion transport (***Adv. Funct. Mater.*** **2022, 32, 2207140**).
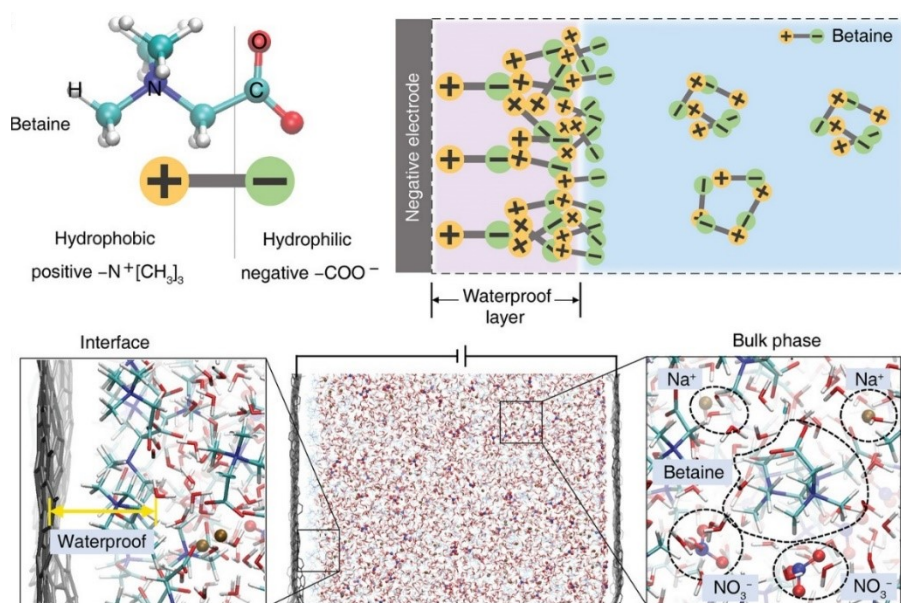


(***Adv. Funct. Mater.*** **2022, 32, 2207140**)

2. Due to the strong interaction induced by more charge transfer between the carboxyl group of zwitterion and the bare Zn atoms, the introduction of zwitterion will preferentially adsorb on the zinc surface (**Figure 7d**) and zwitterion chemically absorbs (COO-Zn) on the Zn surface instead of weakly physically absorbs (***Adv. Funct. Mater.*** **2022, 32, 2207140; *ACS Nano 2023*, 17, 552–560; *Chem. Commun.*, 2022,58, 8504-8507**). Such a strong chemical adsorption introduces a water-poor electrical double layer (EDL), which can effectively inhibit the competitive adsorption of $H_2O$ and its subsequent induced side reactions (***J. Am. Chem. Soc.*** **2022, 144, 19344–19352; *ACS Nano 2023*, 17, 552–560; *ACS Energy Lett.* 2022, 7, 1719−1727; *Nano Energy* 2022, 98, 107220; *Energy Environ. Sci.*, 2022, 15, 4748–4760**).

3. H$_2$ evolution primarily originates from solvated water, rather than free water without interaction with Zn$^{2+}$, and a H$_2$O-poor environment mainly represents low water activity of hydrated Zn$^{2+}$ (*Adv. Mater.* **2022**, *34*, **2206754**). In our work, the CP/EGZn/betaine hydrogel layer significantly deplete the water molecules in the solvation sheath Zn$^{2+}$ ions, largely reducing water activity of hydrated Zn$^{2+}$, coupled with the physical-blocking function to isolate the Zn electrodes from water.



**Figure S43.** Temperature-dependent electrochemical performances of the ZIC based on CP/EGZn/betaine hydrogel electrolytes: a1-a7) CV and b1-b7) GCD curves at different temperatures; c) CV profiles at 50 mV s$^{-1}$; d) GCD curves recorded at 0.5 A g$^{-1}$.

**Figure S44.** a) Nyquist plots of ZICs with CP/EGZn/betaine hydrogel electrolytes under −40, −20, 0, 20, 40, 60, and 80 °C, respectively. Rate performance at b) low temperature and c) high temperature.
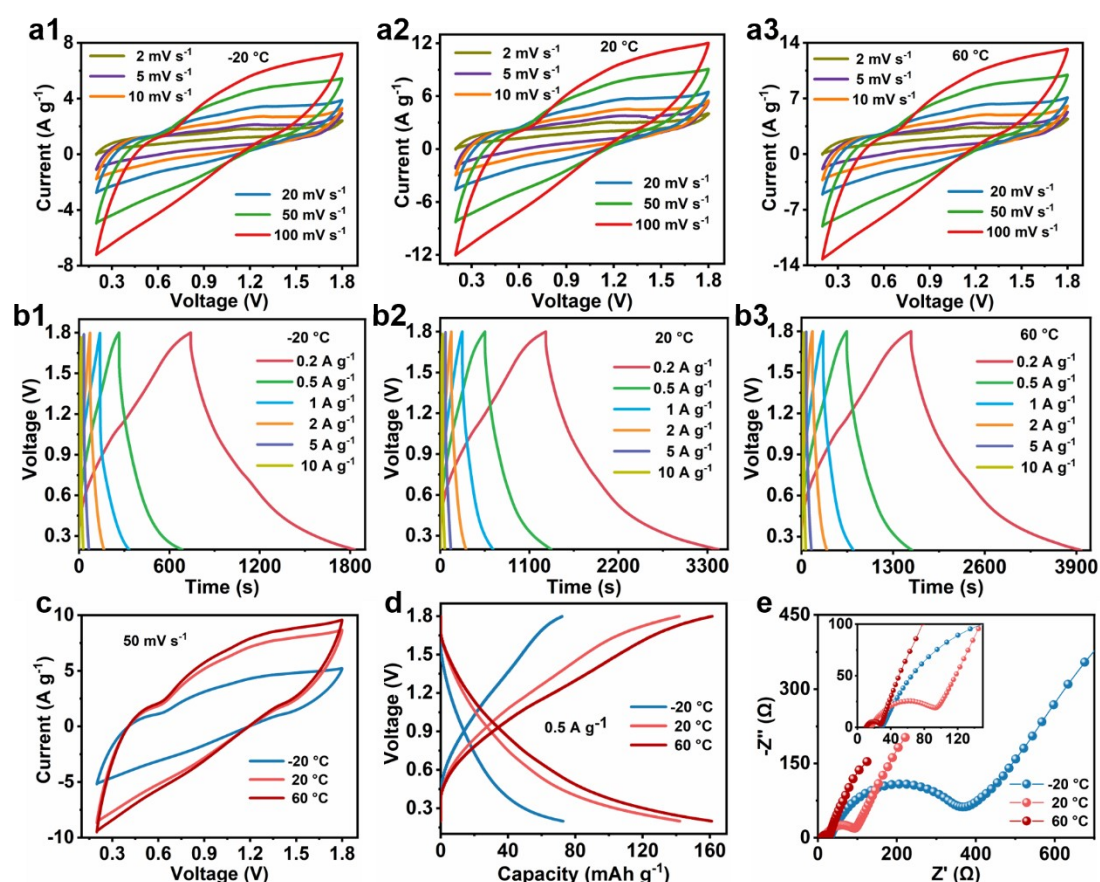


**Figure S45.** Temperature-dependent electrochemical performances of the ZIC based on CP/EGZn/proline hydrogel electrolytes: a1-a3) CV and b1-b3) GCD curves at different temperatures; c) CV profiles at 50 mV s$^{-1}$; d) GCD curves recorded at 0.5 A g$^{-1}$; e) Nyquist plots.
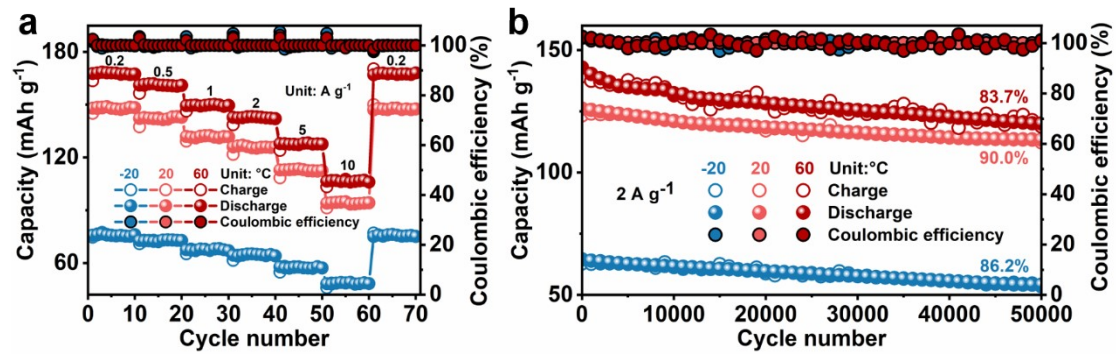
**Figure S46.** a) Rate performance and b) cycling stability of ZICs with CP/EGZn/ proline hydrogel electrolytes at different temperatures.
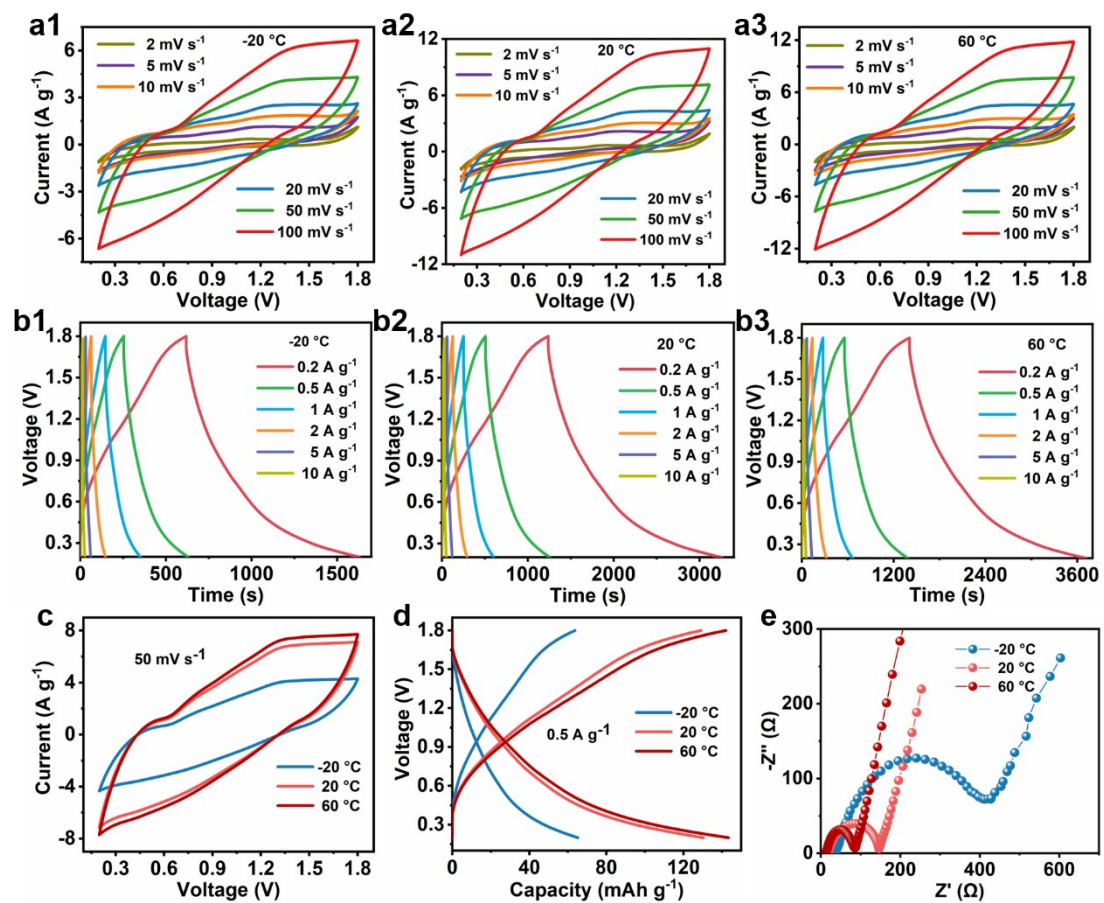


**Figure S47.** Temperature-dependent electrochemical performances of the ZIC based on CP/EGZn/DMG hydrogel electrolytes: a1-a3) CV and b1-b3) GCD curves at different temperatures; c) CV profiles at 50 mV s$^{-1}$; d) GCD curves recorded at 0.5 A g$^{-1}$; e) Nyquist plots.
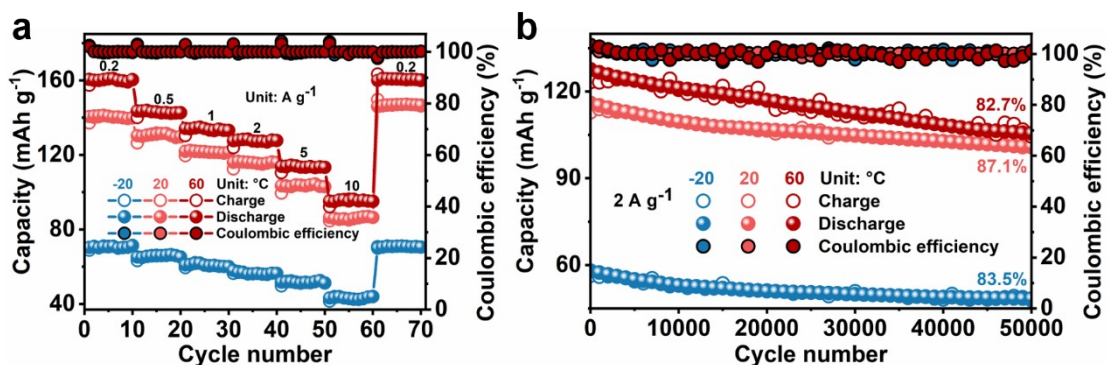
**Figure S48.** a) Rate performance and b) cycling stability of ZICs with CP/EGZn/ DMG hydrogel electrolytes at different temperatures.
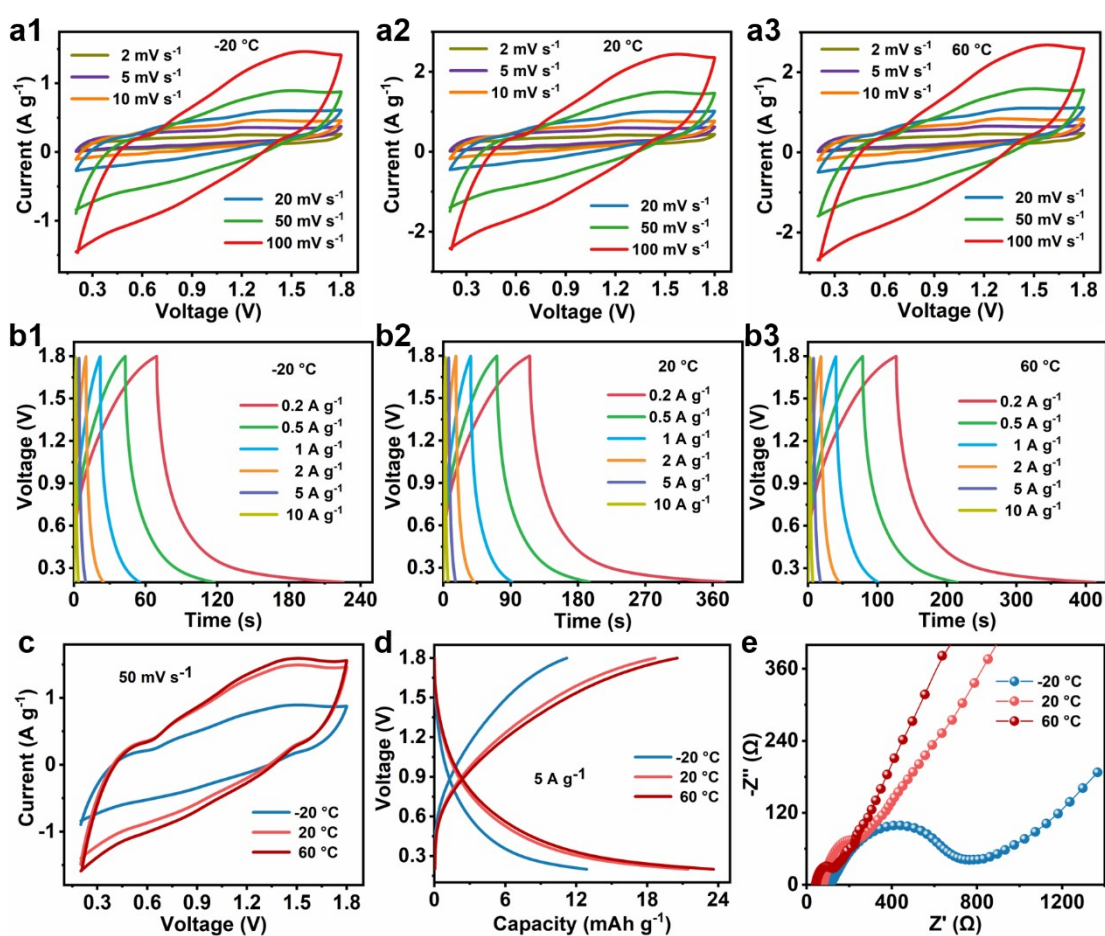


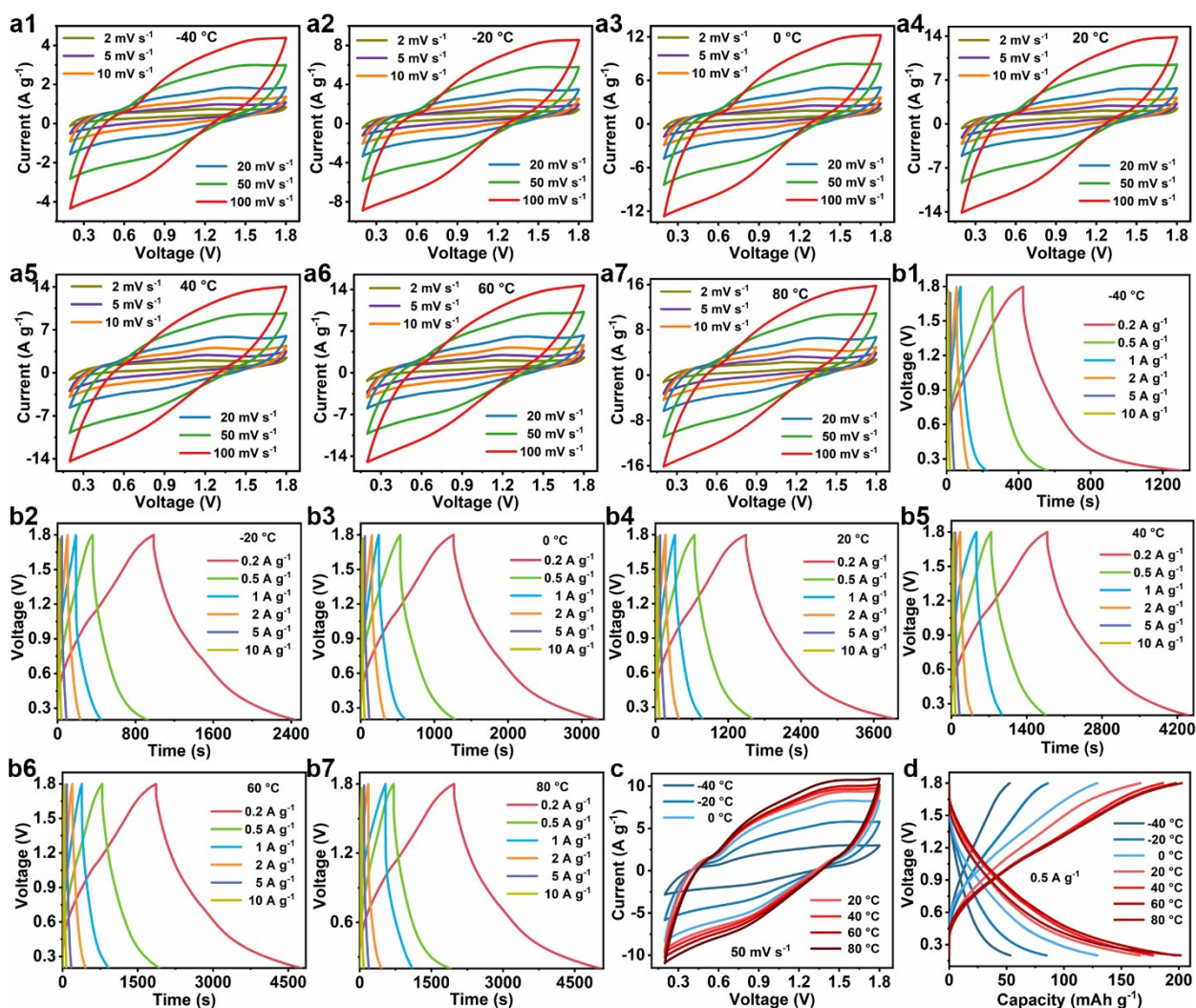**Figure S49.** Temperature-dependent electrochemical performances of the ZIC based on CP/EGZn hydrogel electrolytes: a1-a3) CV and b1-b3) GCD curves at different temperatures; c) CV profiles at 50 mV s$^{-1}$; d) GCD curves recorded at 0.5 A g$^{-1}$; e) Nyquist plots.
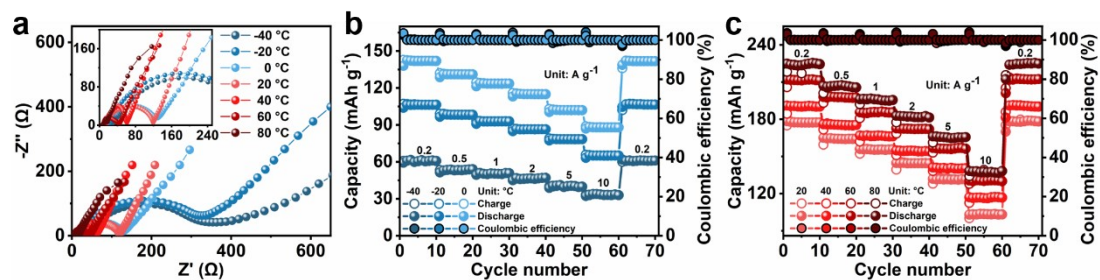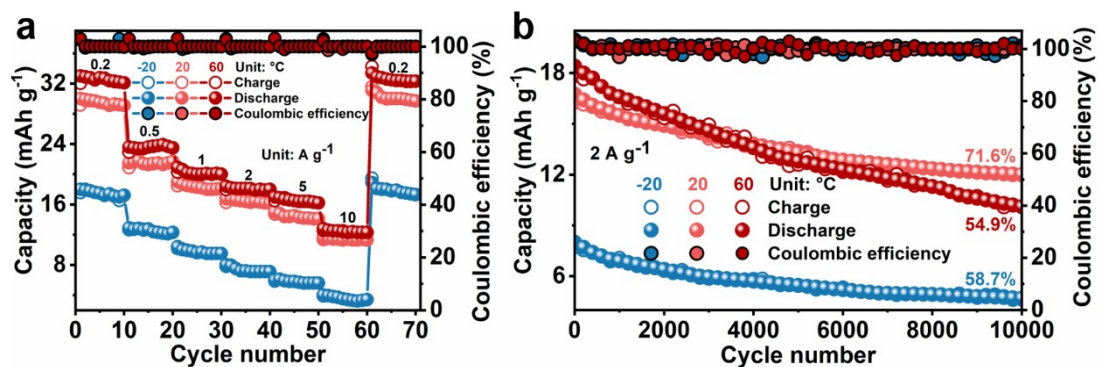
**Figure S50.** a) Rate performance and b) cycling stability of ZICs with CP/EGZn hydrogel electrolytes at different temperatures.
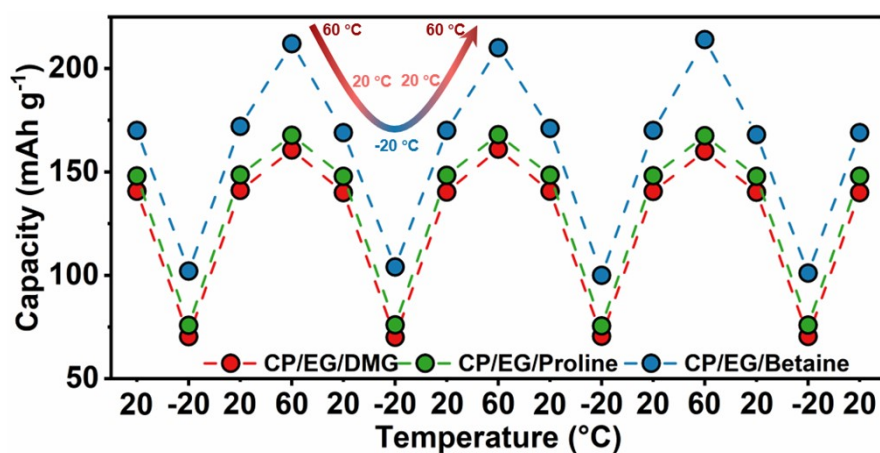


**Figure S51.** Cyclic testing of ZICs with SZHEs under 60, 20, −20, −20, and 60 °C at 0.2 A g$^{-1}$, respectively.
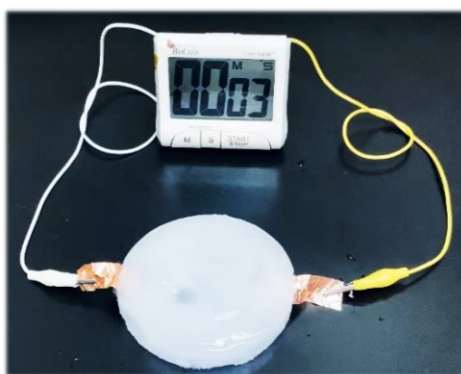


**Figure S52.** Digital images of the EA ZIC when sealed into an ice cube, powering an electronic watch.
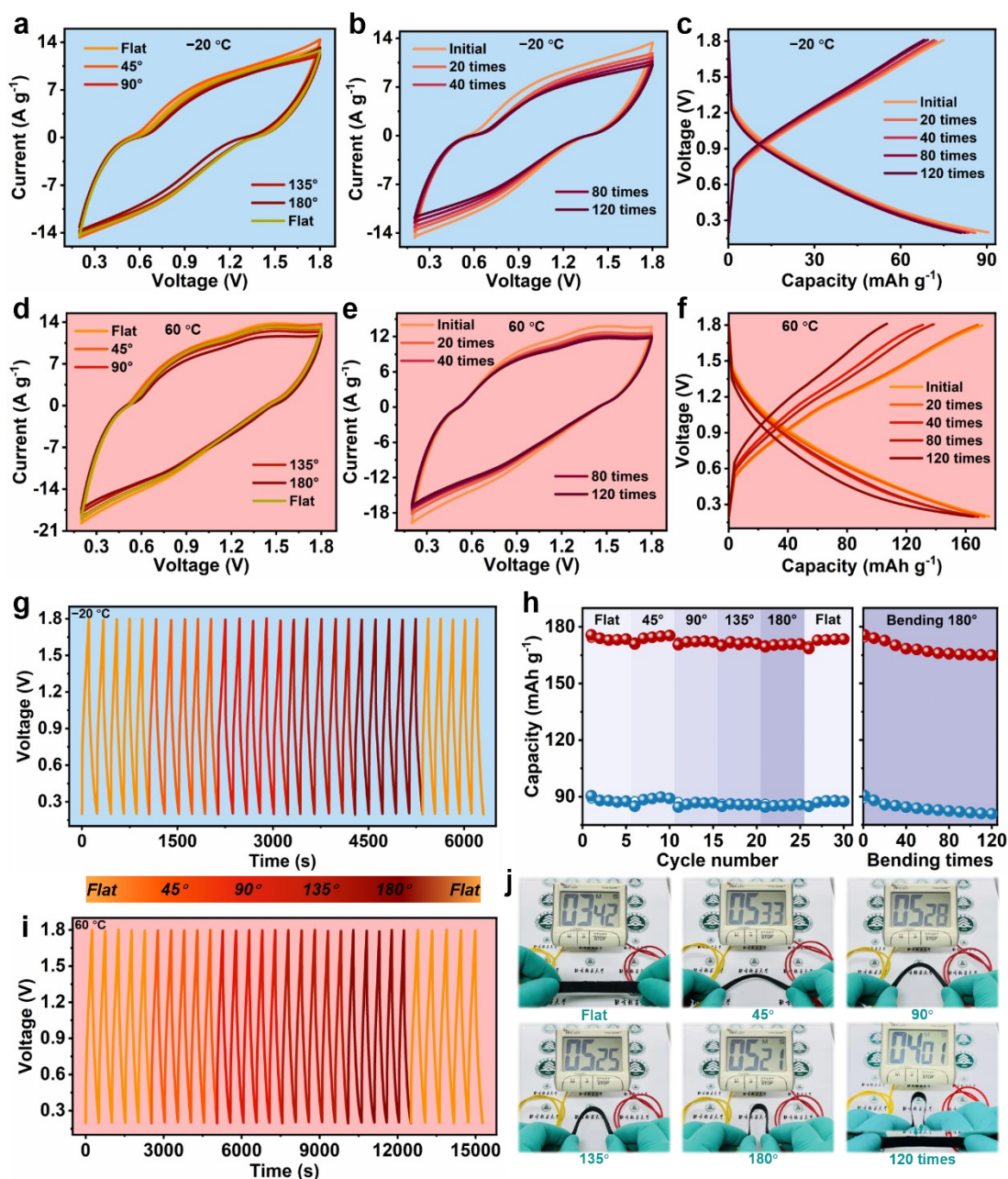
**Figure S53.** a,g) CV and d,i) GCD curves of CP/EGZn/betaine ZICs at bending angles of 0°, 45°, 90°, 135°, and 180° under −20 °C and 60 °C, respectively. b,e) CV and c,f) GCD curves of CP/EGZn/betaine ZICs at repeated 180° bending cycles under −20 °C and 60 °C, respectively. h) Capacity evolution of CP/EGZn/betaine ZICs in the different bent states and following repeated 180° bending cycles at −20 °C and 60 °C, respectively. j) Demonstration of powering a timer at bending angles of 0°, 45°, 90°, 135°, and 180° as well as repeated 180° bending cycles.
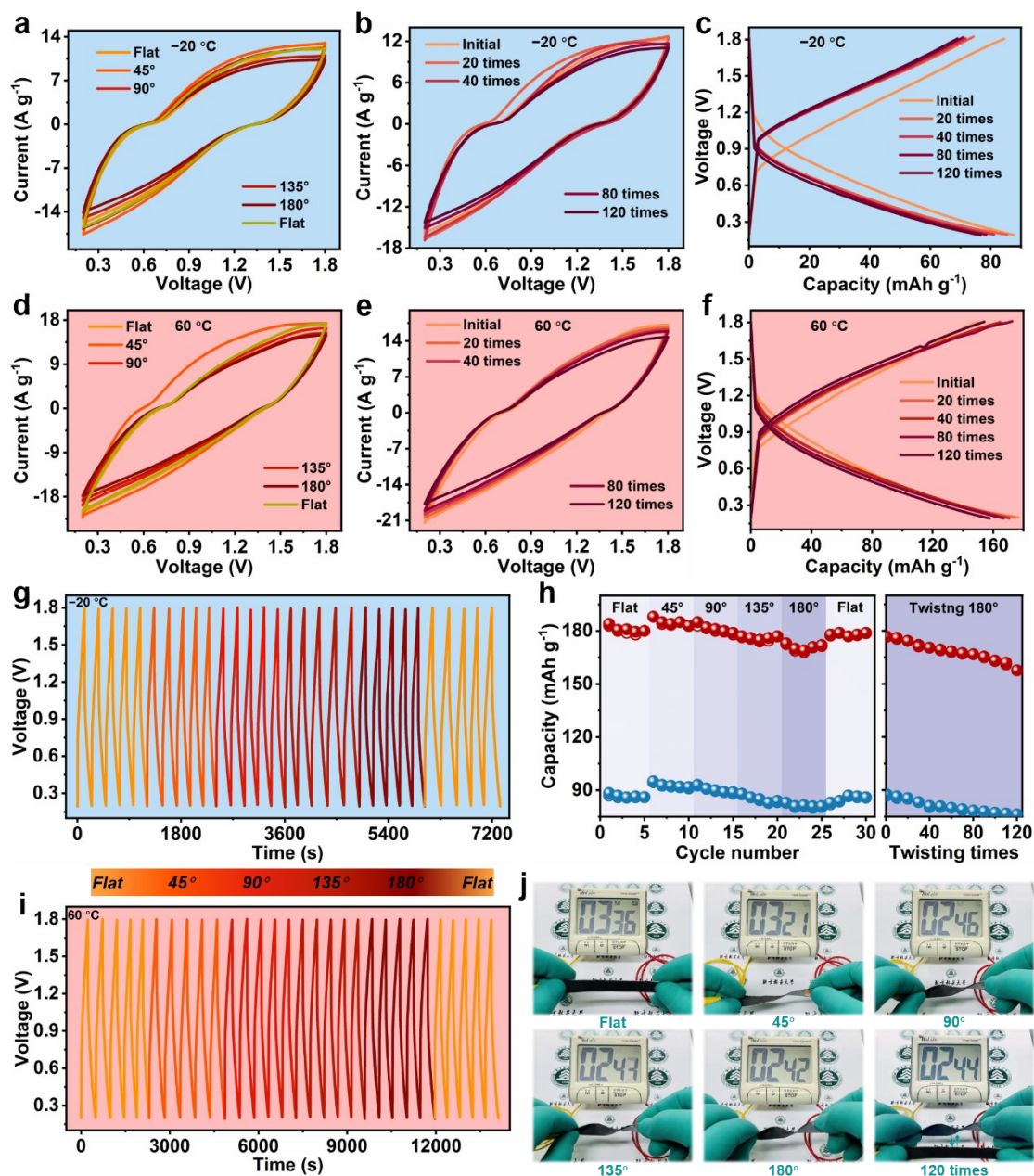
**Figure S54.** a,g) CV and d,i) GCD curves of CP/EGZn/betaine ZICs at twisting angles of 0°, 45°, 90°, 135°, and 180° under −20 °C and 60 °C, respectively. b,e) CV and c,f) GCD curves of CP/EGZn/betaine ZICs at repeated 180° twisting cycles under −20 °C and 60 °C, respectively. h) Capacity evolution of CP/EGZn/betaine ZICs in the different twisted states and following repeated 180° twisting cycles at −20 °C and 60 °C, respectively. j) Demonstration of powering a timer at twisting angles of 0°, 45°, 90°, 135°, and 180° as well as repeated 180° twisting cycles.
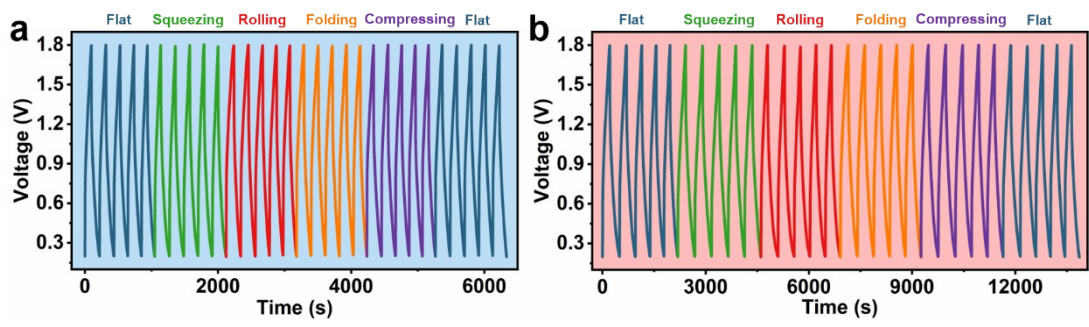
**Figure S55.** GCD curves of the flexible ZICs with CP/EGZn/betaine hydrogel electrolytes under various dynamic deformations at a) −20 °C and b) 60 °C.
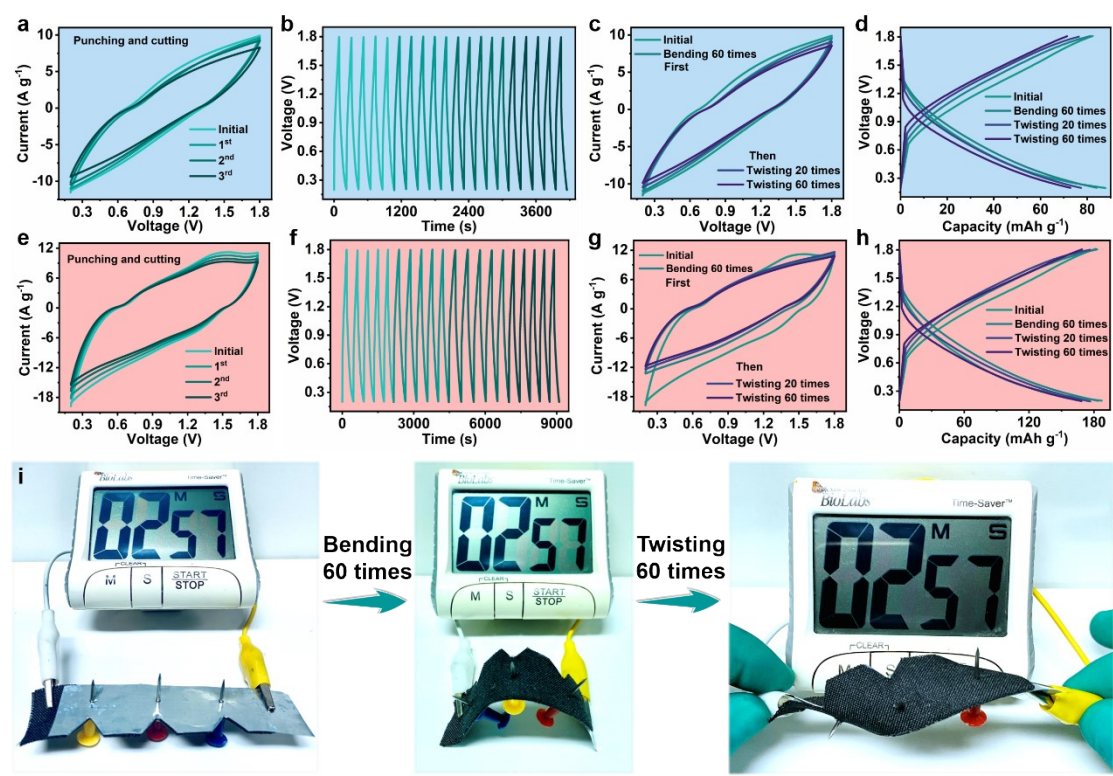


**Figure S56.** a,e) CV and b,f) GCD curves of the flexible ZICs with CP/EGZn/betaine hydrogel electrolytes at different punching and cutting times under −20 and 60 °C, respectively. c,g) CV and d,h) GCD curves of the flexible ZICs with 3 times of punching and cutting in the following repeated bending and twisting cycles at −20 °C and 60 °C, respectively. i) An electronic watch powered by the flexible ZICs with 3 times of punching and cutting under repeatedly bending and twisting deformation.
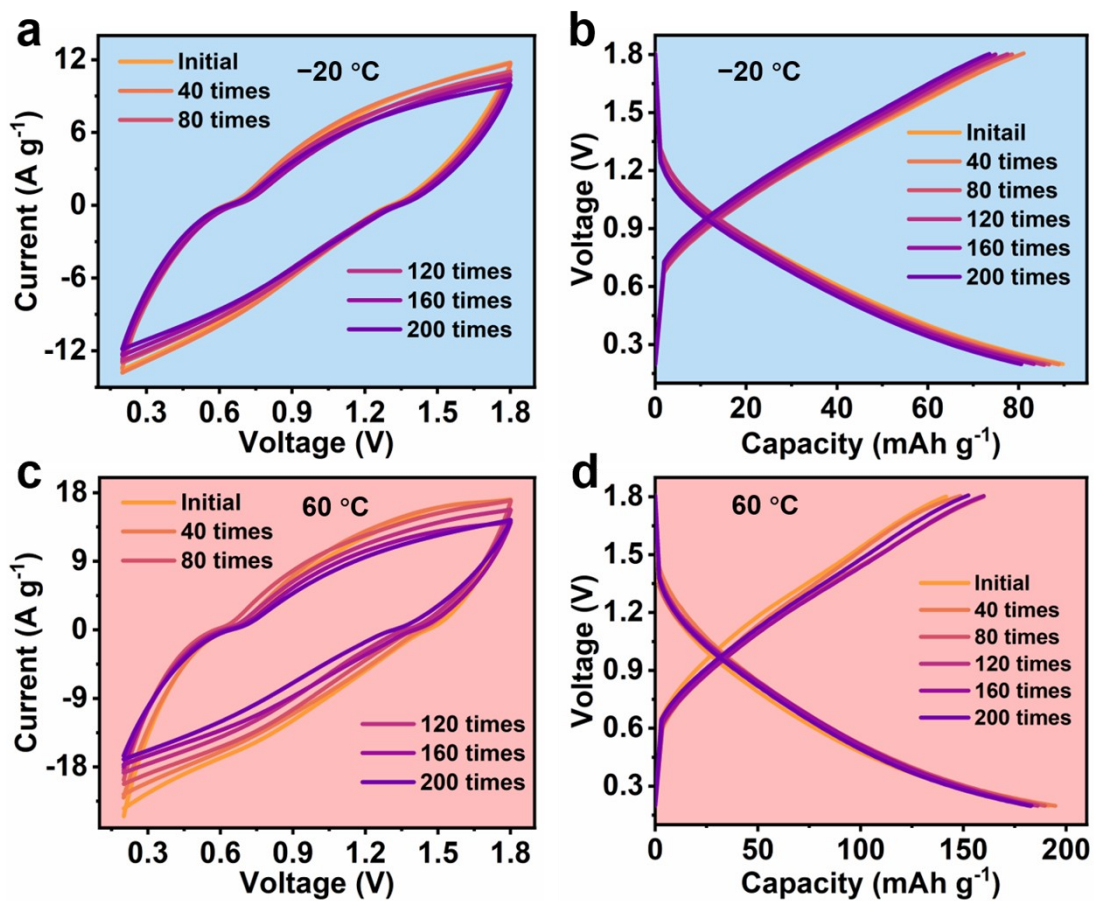
**Figure S57.** a,c) CV and b,d) GCD curves of the flexible ZICs with CP/EGZn/betaine hydrogel electrolytes at different hammering times under −20 and 60 °C, respectively.
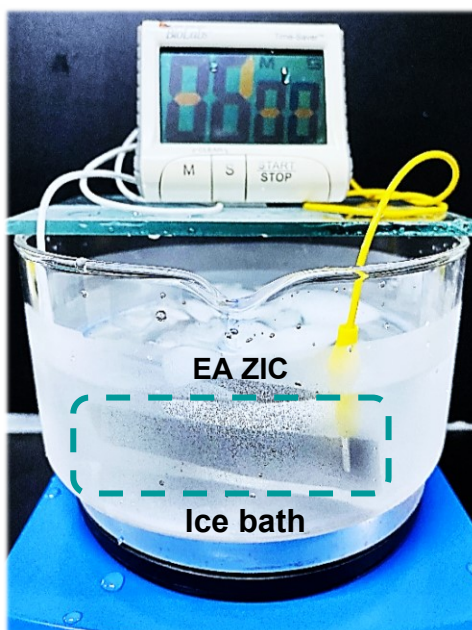


**Figure S58.** The EA ZIC is still capable to power an electronic watch after ice bath washing for over 10 min.
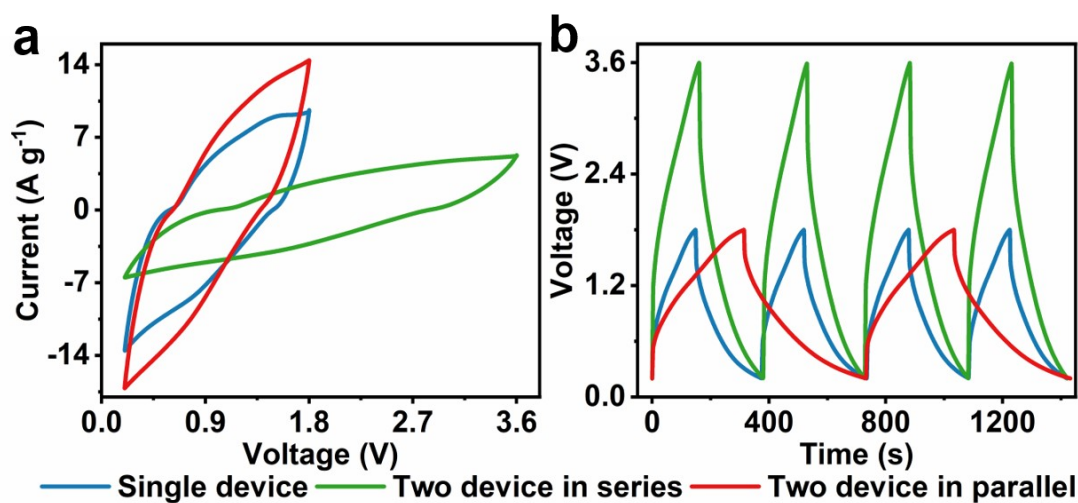
**Figure S59**. a) CV (50 mV s$^{-1}$) and b) GCD (2 A g$^{-1}$) curves of the single and two-in-series ZICs.
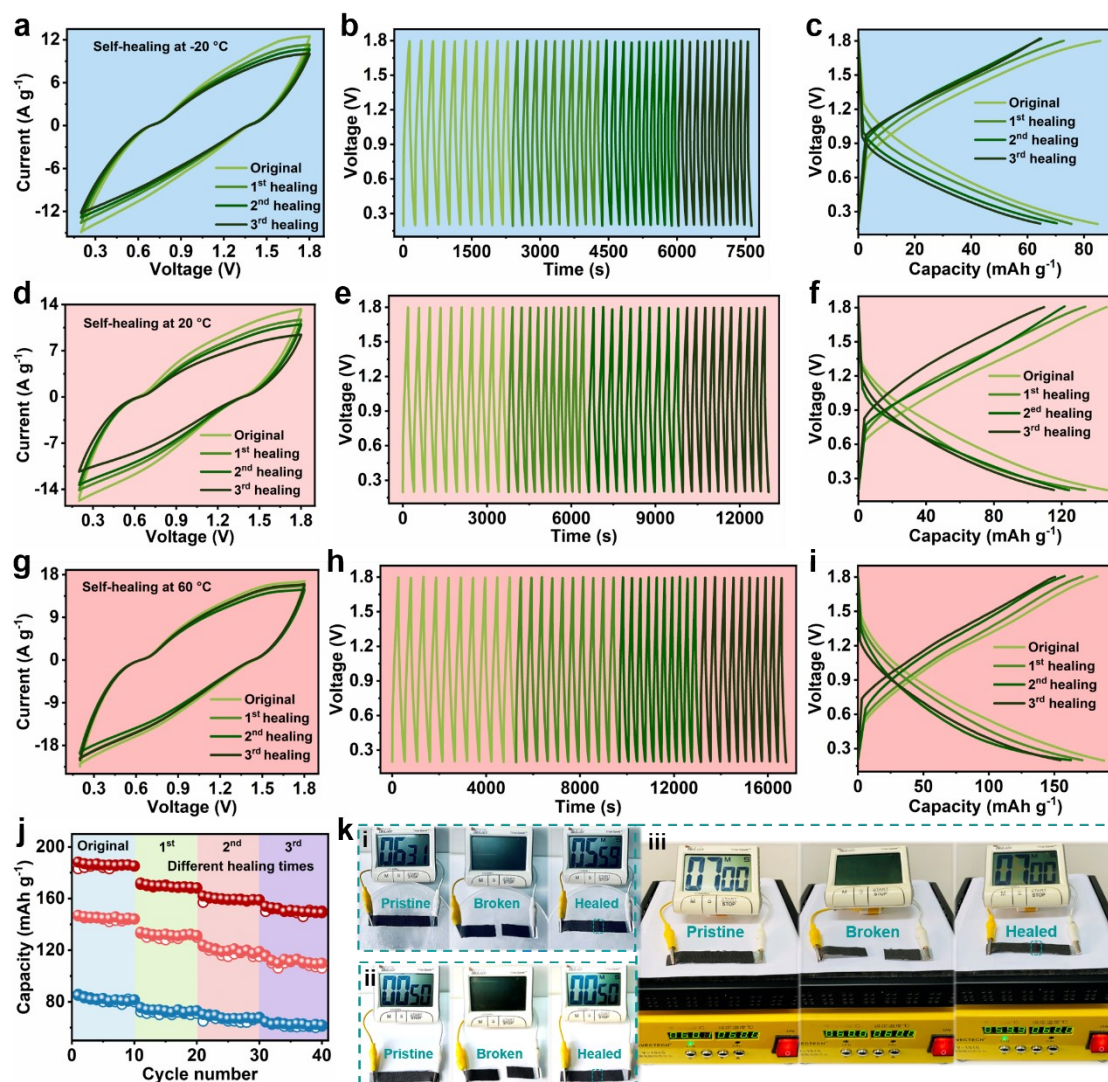
**Figure S60.** a,d,g) CV, b,c,e,f,h,i) GCD curves, and j) capacity evolution for the CP/ EGZn/betaine ZICs after three continuous cutting/self-healing cycles at −20, 20, and 60 °C, respectively. k) Photographs of the self-healing aqueous ZICs powering a clock before cutting (left), after cutting (middle), and after self-healing (right) at i) −20, ii) 20, and iii) 60 °C, respectively.



**Supramolecular Zwitterionic HE**

- Integrated multiple functions
- Top-class $\sigma$ and $t_{Zn}^{2+}$
- Structural integrity
- Suppression of Zn dendrite growth and side reactions
- Self-healing interface
- Safe operation in various harsh environments
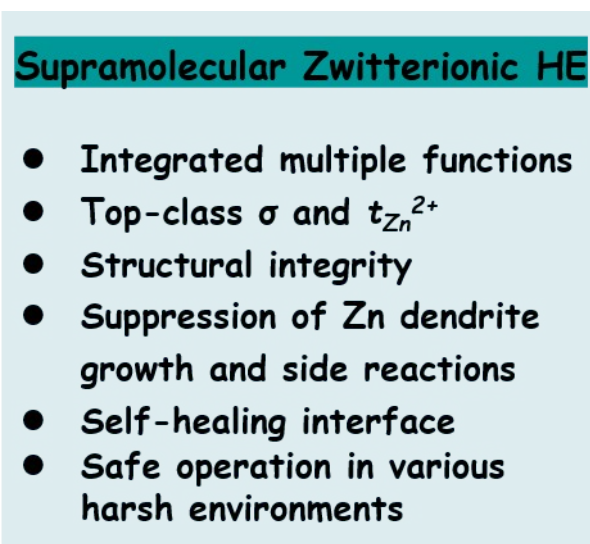
**Figure S61.** Schematic depicting the advantages of the SZHEs in ZIC applications.
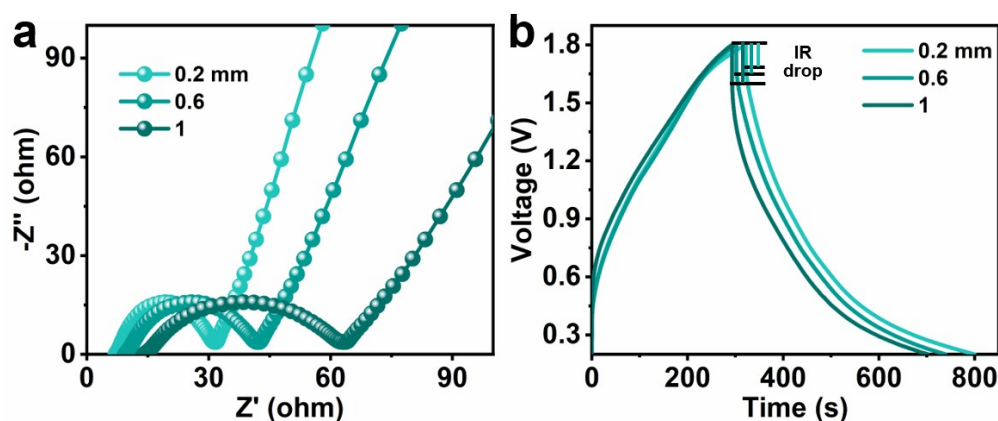


**Figure S62.** (a) Nyquist plots and (b) GCD curves of ZICs based on the CP/EGZn/ betaine with different thickness (IR: inner resistance).

**Figure S63.** A customize mold is used to tailor the thickness of a hydrogel specimen.
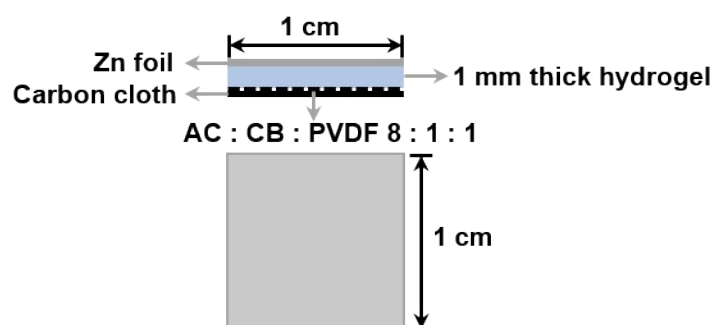


**Figure S64.** Structural details of flexible quasi-solid-state ZICs. (Top) side view and (bottom) top view. Each ZICs contain 180 mg of Zn, 115-120 mg of hydrogel electrolytes (depending on salts and their concentrations), 0.8 mg AC, 15 mg carbon cloth, and 0.2 mg other dry materials.

Please note that we have calculated the device energy and power density based on the mass of activated carbon. This is similar to all other studies on ZICs (***Angew. Chem. Int. Ed.* 2021, 60, 990–997**). The overall device performance based on the total dry mass of devices can be further improved by optimizing the mass of Zn electrodes and hydrogel electrolytes.
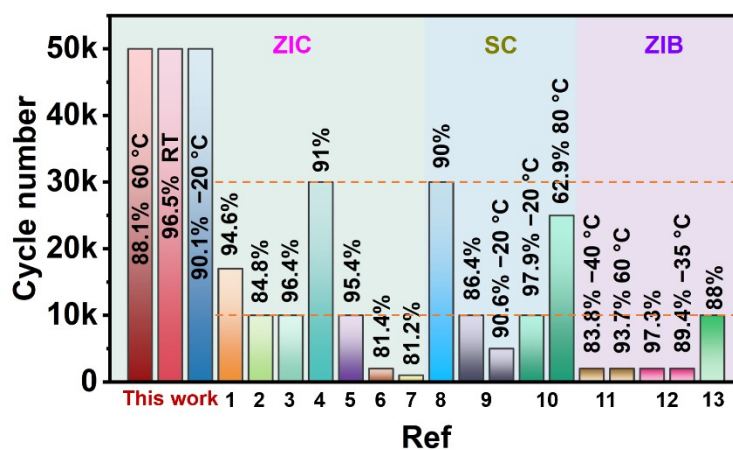
**Figure S65.** Cycling comparison of ZICs, SC, and ZIBs based on HEs.

**Ref.1** Adv. Energy Mater. **2022**, 2202219.
**Ref.2** Small, **2022**, 18, e2200055.
**Ref.3** J. Mater. Chem. A, **2021**, 9, 23941–23954.
**Ref.4** Energy Environ. Mater., **2022**. DOI: 10.1002/eem2.12357.
**Ref.5** ACS Appl. Mater. Interfaces, **2022**, 14, 23452–23464.
**Ref.6** Chem. Eng. J., **2021**, 413, 127502.
**Ref.7** J. Energy Storage, **2022**, 46, 103858.
**Ref.8** Adv. Funct. Mater., **2020**, 31, 2008185.
**Ref.9** Small, **2021**, 17, e2103091.
**Ref.10** Adv. Funct. Mater., **2020**, 30, 2007291.
**Ref.11** Adv. Mater., **2021**, 33, e2007559.
**Ref.12** J. Mater. Chem. A, **2020**, 8, 6828-6841.
**Ref.13** Chem. Eng. J., **2022**, 434, 134646.
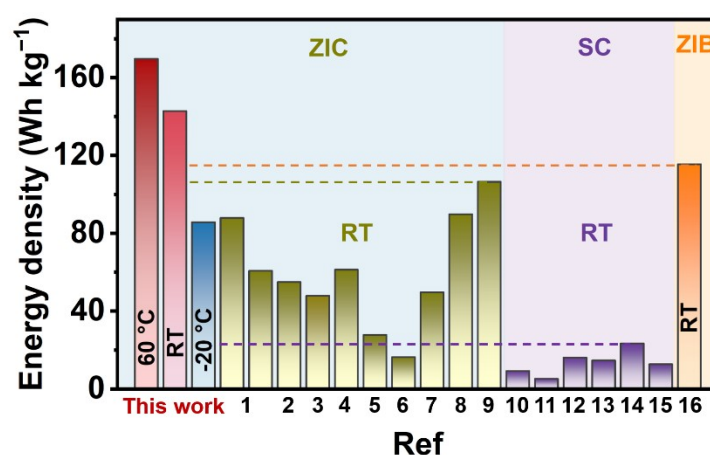
**Figure S66.** Energy comparison of ZICs, SC, and ZIBs based on HEs.

**Ref.1** Small, **2022**, 18, e2200055.
**Ref.2** J. Mater. Chem. A, **2021**, 9, 23941 –23954.
**Ref.3** Energy Environ. Mater., **2022**. DOI: 10.1002/eem2.12357.
**Ref.4** ACS Appl. Mater. Interfaces, **2022**, 14, 23452–23464.
**Ref.5** Chem. Eng. J., **2021**, 413, 127502.
**Ref.6** Adv. Funct. Mater., **2020**, 31, 2008185.
**Ref.7** Adv. Energy Mater. **2022**, 2202219.
**Ref.8** J. Mater. Chem. A, **2022**,10, 12856-12868.
**Ref.9** Adv. Sustainable Syst. **2021**, 2100191.
**Ref.10** Carbohyd. Polym. **2022**, 293, 119673.
**Ref.11** J Power Sources **2019**, 426, 47–54.
**Ref.12** J. Mater. Chem. A, **2020**, 8, 6219-6228.

**Ref.13** Chem Eng J **2021**, 413, 127446.
**Ref.14** ACS Appl. Energy Mater. **2020**, 3, 1944.
**Ref.15** ACS Appl. Mater. Interfaces **2020**, 12, 53164.
**Ref.16** Energy Storage Mater. **2022**, 44, 517–526.

**Toward long-life and high-energy quasi-solid-state zinc-ion capacitors.** Achieving long-life and higher specific energy has been considered a major challenge for quasi-solid-state zinc-ion capacitors (ZICs). In this study, one particular note is the ultralong cycling life (50k) obtained for the ZICs with SZHEs even at low/high temperature, exceedingly outperforms that of the state-of-the-art hydrogel electrolyte-based ZICs, Supercapacitor (SC), and Zinc-Ion Batteries (ZIBs) at room temperature (**Figure S65; Figure S66; Table S4**), demonstrating its extraordinary stability. The specific energy and power of ZICs at 60, room temperature (RT), and –20 °C were calculated based on the weight of the anode, cathode, and solid electrolytes using Ragone-type plot. The ZICs with SZHEs exhibited high specific energy of 169.7 Wh kg$^{-1}$ at 60 °C and maintained a high specific energy of 142.8 Wh kg$^{-1}$ at room temperature and 85.68 Wh kg$^{-1}$ at –20 °C. These performances of the ZICs with SZHEs, which is paired with thin Zn metal and activated carbon (AC)-loaded carbon cloth, are either are significantly higher than that of the previously reported SCs or comparable to that of the ZIB at room temperature using the state-of-the-art hydrogel electrolyte (**Figure S65; Figure S66; Table S4**).

**Supplementary Note 8**
**Lack of pieces about new electrolytes puzzle (Energy Environ. Sci., 2020,13, 4625-4665):**

1. **In-depth understanding of electrolytes:** Although an electrolyte has a great impact on ZICs and ZIBs, investigations on the **structure of the electrolyte, electrochemical in situ state of electrolytes, relationship between the electrolyte and electrochemical performance, and practical considerations** of electrolytes are still in their infancy. Therefore, it is very important to have an in-depth understanding and exploration of these aspects.

2. **Toward cost-effective and innovative electrolytes:** Currently, the low ion transference number, low electrochemical stability, narrow ESPW, and narrow temperature window have largely hindered the development of aqueous electrolytes. Although some novel electrolytes such as ionic liquid electrolyte and organic electrolyte have been explored, their practical applications are still

impeded by some critical issues such as either high cost or low ionic conductivity and low electrochemical activity. In addition, owing to the low ionic conductivity and interface impedance, the development of solid ZICs and ZIBs electrolyte also faces a big obstacle. To design practical ZICs and ZIBs with high specific energy and long-life stability to meet the actual needs of large-scale energy storage, it is urgent to develop cost-effective and innovative electrolytes. Considering the merits of different electrolyte systems, developing **mixed electrolytes with high electrochemical activity and long-life stability** as an important strategy should be seriously considered. For solid electrolytes, adding some aqueous electrolytes can increase the ionic conductivity and improve the interfacial compatibility. As a bottleneck issue for ZICs and ZIBs, further breakthroughs in energy density should not only pursue complicated innovations in cathode materials, but also pay more attention to electrolyte strategy (**Electrolyte adjustment toward high energy density of ZICs and ZIBs**). Last but not least, to meet the environmental adaptability of large-scale energy storage, functional electrolytes need to be developed (**Functional electrolytes with excellent environmental adaptability**).

3. **Systematic and thorough study of the electrolyte/electrode interfaces (EEI):** Actually, EEIs are critical in determining the overall performance of ZIBs, which are considerably influenced by the electrolytes. However, due to the multiphase, multistep reduction of the intricate interface formation and mysterious ion transfer behavior within the interfaces, it is still insufficient to comprehensively describe the relationship between the electrolytes and EEIs, thereby affecting the battery performance (**Establishment of relationship between electrolyte and EEIs**). The interfacial properties are closely related to the formation of compounds on the surface of the electrode, which can considerably influence the ionic conductivity and mechanical strength. In addition, the physical contact, interfacial compatibility, and electrochemical stability are some important parameters of the interfaces (**In-depth understanding of interfacial effect via advanced characterization methods: these in situ techniques mainly include in situ optical microscopy, FTIR, Raman, UV-vis, SXR, SEM, TEM, and so on, which can precisely track the formation, evolution, and ion transport pathway of the interface**). Therefore, understanding the structure and composition of the EEIs and their evolution, as well as the ion transport mechanism, should be further investigated.

# Section S3 Supplementary Tables

**Table S1.** Comparison chart of currently reported advanced HEs for state-of-the-art zinc-based capacitors and batteries.

| Electrolyte | Mechanical performance | Interfacial adhesion | Self-healing | Low temperature | High temperature | Moisture-preserving | Non-flammable | Ref (Published on) |
|---|---|---|---|---|---|---|---|---|
| All-round HE | 846.5% 2.11 MPa | ✓ | ✓ | −40 °C | 60 °C | ✗ | ✗ | Adv. Mater. **2021**, 33, 2007559 |
| PASHE | 315.4% 27.9 kPa | 18.8 kPa | ✗ | ✗ | ✗ | ✗ | ✗ | Adv. Energy Mater. **2022**, 2202219 |
| AF CSAM-C | 910% 0.25 MPa | ✗ | ✗ | −30 °C | ✗ | ✓ | ✗ | Adv. Mater. **2022**, 34, 2110140 |
| Safe PZHE | 200% Twisting | ✗ | ✓ | Anti-icing | ✗ | ✓ | ✓ | Adv. Funct. Mater. **2020**, 30, 2001317 |
| ZSC-gel | 920% 120 kPa | ✗ | ✗ | ✗ | ✗ | ✓ | ✗ | Adv. Energy Mater. **2020**, 10, 2000035 |
| Water-in-salt HE | 500% 40 kPa | ✗ | ✗ | −20 °C | ✗ | ✓ | ✗ | Angew. Chem. Int. Ed. **2021**, 60, 990–997 |
| PDZ-HE | 1122% 48.8 kPa | ✗ | ✗ | −40 °C | 60 °C | ✗ | ✗ | Adv. Funct. Mater. **2022**, 32, 2112540 |
| Water-in-salt PZHE | 507% 103.7 kPa | 31.5 kPa | ✗ | −60 °C | ✗ | ✓ | ✗ | ACS Nano **2021**, 15, 18469−18482 |
| GG/SA | Twisting | ✗ | ✗ | −20 °C | ✗ | ✓ | ✗ | Energy Stora. Mater., **2021**, 41, 599–605 |
| EG-waPUA/PAM | 900% 60 kPa | ✓ | ✗ | −20 °C | ✗ | ✗ | ✗ | Energy Environ. Sci., **2019**, 12, 706−715 |
| KOH-filled SP-DN | 28 kPa 1626% | 0.7 kPa | ✗ | −50 °C | 100 °C | ✓ | ✗ | Energy Environ. Sci., **2021**,14, 4451-4462 |
| A-PAA HE | 600% 80 kPa | ✗ | ✗ | −20 °C | ✗ | ✓ | ✗ | Angew. Chem. Int. Ed. **2020**, 132, 4823–4829 |
| PAM/EG/W/H$_2$SO$_4$ | 350% 25 kPa | 10.4 kPa | ✗ | −30 °C | ✗ | ✓ | ✗ | Energy Environ. Sci., **2021**,14, 3075-3085 |
| KOH-A-PAA HE | 620% 68 kPa | ✗ | ✗ | −30 °C | 80 °C | ✓ | ✓ | Energy Environ. Sci., **2021**,14, 4926-4935 |
| MC/PAM-PDMC | 1800% 230 kPa | ✗ | ✗ | ✗ | ✗ | ✓ | ✗ | Adv. Mater. **2022**, 34, 2110585 |
| PAM/SA/KI | 600% 14 kPa | ✗ | ✗ | ✗ | ✗ | ✓ | ✗ | Angew. Chem. Int. Ed. **2022**, e202210567 |
| PCEE | 300% 0.28 MPa | 21.5 J m$^{-2}$ | ✗ | ✗ | 60 °C | ✗ | ✗ | Nature **2022**, 609, E11 |
| **SZHE** | **2150% 70.3 kPa** | **34.3 kPa 800 J m$^{-2}$** | ✓ | **−40 °C** | **80 °C** | ✓ | ✓ | **This work** |

**Table S2.** Comparison chart of currently reported advanced HE central indicators and new function.

| Electrolyte | Ion migration channel | σ at RT (mS cm$^{-1}$) | $t_{Zn}^{2+}$ | Interfacial repairing | Ref (Published on) |
|---|---|---|---|---|---|
| All-round HE | ✗ | 32.3 | ✗ | ✗ | Adv. Mater. **2021**, 33, 2007559 |
| PASHE | ✓ | 32.9 | 0.84 | ✗ | Adv. Energy Mater. **2022**, 2202219 |
| AF CSAM-C | ✗ | 21.7 | 0.76 | ✗ | Adv. Mater. **2022**, 34, 2110140 |
| Safe PZHE | ✓ | 32 | 0.656 | ✗ | Adv. Funct. Mater. **2020**, 30, 2001317 |
| ZSC-gel | ✓ | 24.6 | ✗ | ✗ | Adv. Energy Mater. **2020**, 10, 2000035 |
| P(SBMA-co-AA)/Zn(CF$_3$SO$_3$)$_2$ | ✓ | 27.6 | ✗ | ✗ | J. Mater. Chem. A, **2022**, 10, 12856−12868 |
| EG-waPUA/PAM | ✗ | 16.8 | ✗ | ✗ | Energy Environ. Sci., **2019**, 12, 706−715 |
| PZIB | ✓ | 21.88 | 0.74 | ✗ | Adv. Sci. **2022**, 9, 2104832 |
| ADC-gel | ✓ | 6.48 | 0.604 | ✗ | Nano-Micro Lett. **2022**,14, 93 |
| MorphGE | ✗ | 26.2 | 0.65 | ✗ | Nano Res. **2022**, 15, 2030−2039 |
| ZIS–PVA | ✓ | 10.3 | ✗ | ✗ | J. Mater. Chem. A, **2021**,9, 24325−24335 |
| PSX HE | ✗ | 18.86 | 0.8 | ✗ | Energy Stora.Mater., **2022**, 51 588−598 |
| SZHE | ✓ | 48 | 0.86 | ✓ | This work |

**$\sigma$: Ionic conductivity; $t_{Zn}^{2+}$: Zn-ion transference number.**

These comparisons (**Table S3**) clearly confirm the novelty of our well-designed all-around supramolecular zwitterionic hydrogel electrolytes with ion migration channels. Therefore, we firmly believe that this is the first demonstration of the SZHEs that simultaneously achieves a wide set of demanding properties with a high level of success for state-of-the-art zinc-ion capacitors. It should be noted that none of the previously reported zwitterion-based hydrogel electrolytes, have achieved a comparable level of success. In particular, achievement of interfacial repairing has never been reported in other hydrogel electrolytes. The true novelty of this study is the design of all-around supramolecular zwitterionic hydrogel electrolytes with ion migration channels that allows for an unprecedented combination of mechanical, electrochemical, interfacial, and thermal properties for safe operation of ZICs. Mostly importantly, we found the missing pieces of the zwitterion de-solvation puzzle and quantified the number of water molecules near $Zn^{2+}$.

**Table S3.** Various comparisons with zwitterion-based hydrogel electrolytes reported in recent studies.

| Zwitterion HE | Performance | | | | | | | Mechanism | | Application | | | | | Ref |
|---|---|---|---|---|---|---|---|---|---|---|---|---|---|---|---|
| | Mechanics | Adhesion | Healing | Tem (°C) | σ at RT (mS cm⁻¹) | $t_{Zn}^{2+}$ | Nonflammable | Interfacial repairing | De-solvation | Self-healing | Mechanical shock | Extreme environment | Cycling Energy (Wh kg⁻¹) | Demonstration | |
| SAS ZIB | 591.5% 131.2 kPa | ✗ | ✗ | −20 | 13.65 | ✗ | ✗ | ✗ | ✗ | ✗ | ✗ | ✗ | 1000 N/A | LED light Phone | ACS Appl. Energy Mater. 2022, 5, 7530−7537 |
| PAA-co-PDP SC | 2880% 80 kPa | ✗ | ✓ | RT | 9.4 | ✗ | ✗ | ✗ | ✗ | ✗ | ✗ | ✗ | ✗ | ✗ | ACS Appl. Mater. Interfaces 2022, 14, 9608−9617 |
| PolyAS-EG SC | ~1390.1% ~21.3 kPa | ✗ | ✗ | -50 | 1.51 at -50 ℃ | ✗ | ✗ | ✗ | ✗ | ✗ | ✗ | ✗ | 10 000 N/A | LED lights | Adv. Sci. 2022, 9, 2201679 |
| PASHE ZIC | 315.4% 27.9 kPa | 18.8 kPa | ✗ | RT | 32.9 | 0.84 | ✗ | ✗ | ✓ | ✗ | ✗ | ✗ | 17 000 N/A | Electronic watch Sensors | Adv. Energy Mater. 2022, 12, 2202219 |
| Safe PZHE ZIB | 200% Twisting | ✗ | ✓ | Anti-icing | 32 | 0.656 | ✓ | ✗ | ✗ | ✓ | Cut Hammer | Washing Ice、burning | 600 N/A | Electronic watch | Adv. Funct. Mater. 2020, 30, 2001317 |
| ZSC-gel ZIB | 920% 120 kPa | ✗ | ✗ | RT | 24.6 | ✗ | ✗ | ✗ | ✗ | ✗ | ✗ | ✗ | 10 000 386 | Smart watch LEDs | Adv. Energy Mater. 2020, 10, 2000035 |
| ZIS-PVA ZIB | 310 kPa | ✗ | ✗ | RT | 10.3 | ✗ | ✗ | ✗ | ✗ | ✗ | Puncture | ✗ | 600 N/A | LEDs Electronic watch | J. Mater. Chem. A, 2021,9, 24325-24335 |
| PAB-Zn ZIC | 20 kPa 1605 % | 359.4 N/m | ✓ | RT | N/A | ✗ | ✗ | ✗ | ✗ | Yes | Cut | ✗ | 4000 260 | Electronic watch | Chem. Eng. J. 2023, 452, 139014 |
| Water-in-salt PZHE (ZIC) | 507% 103.7 kPa | 31.5 kPa | ✗ | -60 | 74.3 | ✗ | ✗ | ✗ | ✗ | ✗ | Fold&Cut Hammer | Wash Ice | 100 000 253.0 | Timer Electronic bracelet | ACS Nano 2021, 15, 18469−18482 |
| PolySH SC | 325% 5 kPa | ✗ | ✗ | −40 60 | 12.6 at -40 ℃ | ✗ | ✗ | ✗ | ✗ | ✗ | Puncture | Ice | 10 000 N/A | LED lamp | Adv. Funct. Mater. 2021, 31, 2009438 |
| SPS–Zn ZIC | 310.2% 61.8 kPa | 4.1 kPa | ✗ | −20 | 25 | 0.64 | ✗ | ✗ | ✗ | ✗ | ✗ | Ice | 12 000 ~52 | LED Timer | J. Mater. Chem. A, 2022, 10, 25701-25713 |
| P(SBMA-co-AA)/Zn(CF₃SO₃) ZIC | 313.4% 22.4 kPa | ✗ | ✗ | RT | 27.6 | ✗ | ✗ | ✗ | ✗ | ✗ | ✗ | ✗ | 10 000 89.8 | LED Mobile phone | J. Mater. Chem. A, 2022, 10, 12856-12868 |
| (P(A-coS)@PAM SC | 80% strain | ✗ | ✗ | RT | N/A | ✗ | ✗ | ✗ | ✗ | ✗ | 50% compression strain | Acid Alkali | 4000 N/A | Electroluminescent glass | Small Methods 2023, 2201448 |
| ADC-gel ZIB | N/A | ✗ | ✓ | RT | 6.48 | 0.604 | ✗ | ✗ | ✗ | ✓ | Cut Hammer | Soaking | N/A | LED | Nano-Micro Lett. 2022, 14, 93 |
| PSPE ZIB | 203.1% 19.8 kPa | ✓ | ✗ | −20 80 | 7.1 | ✗ | ✗ | ✗ | ✗ | ✗ | ✗ | ✗ | 500 165 | LED lit up | J. Mater. Chem. A, 2022,10, 17721-17729 |
| SZHE ZIC | 2150% 70.3 kPa | 34.3 kPa 800 J m⁻² | ✓ | -40 80 | 48 | 0.86 | ✓ | ✓ | ✓ | ✓ | Fold&Cut Hammer Puncture | Wash&Boil Ice&Fire | 50 000 142.8 | Wearables Biomedical sensor | This work |

**Table S4.** Comparison of the electrochemical performance of the ZIC in this work with other reported energy storage devices based on different types of HEs.

| HE | type | Working T | Conductivity (mS cm⁻¹) | Cycling stability (cycle) | Energy density (Wh kg⁻¹) | Refs. |
|---|---|---|---|---|---|---|
| CP/EGZn/betaine | | −40 °C | 21 | 50000 (**90.1% −20 °C**) | 85.68 | |
| | | 20 °C | 48 | 50000 (96.5%) | 142.8 | |
| | | 80 °C | 88.9 | 50000 (**88.1 60 °C**) | 169.68 | |
| CP/EGZn/proline | OHE (ZIC) | −40 °C | 19.3 | 50000 (**86.2% −20 °C**) | 60.64 | This work |
| | | 20 °C | 46.5 | 50000 (90%) | 118.4 | |
| | | 80 °C | 79.7 | 50000 (**83.7 60 °C**) | 134.16 | |
| CP/EGZn/DMG | | −40 °C | 18.6 | 50000 (**85.5% −20 °C**) | 56.24 | |
| | | 20 °C | 45 | 50000 (87.1%) | 112.48 | |
| | | 80 °C | 76.7 | 50000 (**82.7 60 °C**) | 128.48 | |
| CTG/ZnSO₄ | OHE (Zn-Mn) | −40 °C | 19.4 | 2000 (83.8%) | 67 mWh cm⁻³ | [7] |
| | | 60 °C | 38.5 | 2000 (93.7%) | 105 mWh cm⁻³ | |
| PVA/GL/ZnCl₂ | OHE (ZIC) | −50 °C | 0.21 | - | - | [8] |
| | | 80 °C | 12.5 | - | - | |
| PAM/GL/LiCl | OHE (SC) | −40 °C | 4.3 | 5000 (**90.6% −20 °C**) | - | [9] |
| | | 25 °C | 13.5 | 10000 (86.4%) | - | |
| PVA-B-G/ZnSO₄ | OHE (Zn-Mn) | −35 °C | 10.1 | 2000 (89.4%) | 46.8 mW h cm⁻³ | [10] |
| | | 25 °C | 29.6 | 2000 (97.3%) | 25.8 mW h cm⁻³ | |
| PAM/LiCl/EG | OHE (SC) | −20 °C | 1.9 | 10000 (97.9%) | 5.83 | [11] |
| | | 80 °C | 51.6 | 25000 (62.9%) | - | |
| PAM-A/GL/ZnSO₄ | OHE (ZIB) | −20 °C | 8.43 | - | - | [12] |
| | | 25 °C | 13.94 | 10000 (88%) | - | |
| PAM-Alginate/EG | OHE (Zn-Mn) | −20 °C | 14.1 | 500 (66%) | 17.5 mW h cm⁻³ | [13] |
| | | 80 °C | 18.2 | - | 29 mW h cm⁻³ | |
| EG-waPUA/PAM | OHE(Zn-Mn) | −20 °C | 14.6 | 600 (74.54%) | 26.2 mW h cm⁻³ | [14] |
| | | 20 °C | 16.8 | 600 (87.41 %) | 32.7 mW h cm⁻³ | |
| PVA-CMC/EG/Zn(CF₃SO₃)₂ | OHE (ZIC) | −20 °C | 7.5 | - | 60.7 | [15] |
| | | 20 °C | 17.3 | 10000 (84.8%) | 87.9 | |
| P(AMPS-AA)/ZnCl₂ | HE (ZIC) | RT | - | 1000 (81.2%) | 205.3 | [16] |
| P(AM-co-AA)/κ-CG/ZnSO₄ | HE (ZIC) | RT | 17.6 | 10000 (96.4%) | 54.9 | [17] |
| PVA-ZnSO₄ | HE (ZIC) | RT | - | 30000 (91%) | 47.86 | [8] |
| PAm/agar/Zn(CF₃SO₃)₂ | HE (ZIC) | RT | 15.5 | 10000 (95.4%) | 61.3 | [18] |
| PAM/ZnSO₄ | HE (ZIC) | RT | - | 2000 (81.4%) | 27.7 | [19] |
| PVA/H₂SO₄ | HE (SC) | RT | - | 30000 (90%) | 16.3 | [20] |

**"RT"**: Room Temperature. **"OHE"**: Organohydrogel Electrolyte. **"HE"**: Hydrogel Electrolyte. **"ZIC"**: Zn-Ion Capacitor. **"SC"**: Supercapacitor. **"Zn-Mn"**: Zn–MnO₂ Battery. **"ZIB"**: Zinc-Ion Battery.

**Table S5.** Summary of the value of $R_s$ and $R_{ct}$ for the ZICs with different SZHEs at various temperatures

| Codes | Temperature (°C) | $R_s$ (Ω) | $R_{ct}$ (Ω) |
|---|---|---|---|
| CP/EGZn/betaine | −40 | 24.6 | 344.3 |
| | −20 | 17.9 | 321.4 |
| | 0 | 13.9 | 128.9 |
| | 20 | 12.2 | 119.3 |
| | 40 | 10.7 | 61 |
| | 60 | 8.1 | 44 |
| | 80 | 5.6 | 17 |
| CP/EGZn/proline | −20 | 28.4 | 364.4 |
| | 20 | 16.1 | 93.3 |
| | 60 | 10.27 | 27.8 |
| CP/EGZn/DMG | −20 | 29.7 | 409.8 |
| | 20 | 17.7 | 147.3 |
| | 60 | 11.7 | 85 |
| CP/EGZn | −20 | 105.1 | 748.2 |
| | 20 | 75.9 | 226.9 |
| | 60 | 43.1 | 121.9 |

## Section S4 Supplementary Movies

**Movie S1**

the inflation process of the CP/EGZn/betaine hydrogel.

**Movie S2**

Self-healing performance of two CP/EGZn/betaine hydrogel electrolytes.

**Movie S3**

Adhesion stability of the CP/EGZn/betaine hydrogel electrolytes upon fire and cold.

**Movie S4**

Anti-heating and freeze-resistant property of EA ZICs.

**Movie S5**

Mechanic-resilient electrochemical functionality of EA ZICs.

**Movie S6**

Hammering tests of EA ZICs at −20 °C.

**Movie S7**

EA ZICs are able to work upon firing.

**Movie S8**

Demonstration of EA ZICs resilience to washing in an ice bath.

**Movie S9**

Successful experimental demonstrations of EA ZICs in combination with electrophysiological sensors.

# Section S5 Supplementary References

1. R. Zhao, H. Wang, H. Du, Y. Yang, Z. Gao, L. Qie and Y. Huang, *Nat. Commun.*, 2022, **13**, 3252.
2. Z. Zhao, J. Zhao, Z. Hu, J. Li, J. Li, Y. Zhang, C. Wang and G. Cui, *Energy Environ. Sci.*, 2019, **12**, 1938–1949.
3. W. Zhang, B. Wu, S. Sun and P. Wu, *Nat. Commun.*, 2021, **12**, 4082.
4. D. Han, C. Cui, K. Zhang, Z. Wang, J. Gao, Y. Guo, Z. Zhang, S. Wu, L. Yin, Z. Weng, F. Kang and Q.-H. Yang, *Nat. Sustain.*, 2022, **5**, 205–213.
5. S. R. Petersen, H. Prydderch, J. C. Worch, C. J. Stubbs, Z. Wang, J. Yu, M. C. Arno, A. V. Dobrynin, M. L. Becker and A. P. Dove, *Angew. Chem. Int. Ed.*, 2022, **61**, e202115904.
6. C. Wang, Z. Pei, Q. Meng, C. Zhang, X. Sui, Z. Yuan, S. Wang and Y. Chen, *Angew. Chem. Int. Ed.*, 2021, **60**, 990–997.
7. M. Chen, J. Chen, W. Zhou, X. Han, Y. Yao and C. P. Wong, *Adv. Mater.*, 2021, **33**, e2007559.
8. Y. Jiang, K. Ma, M. Sun, Y. Li and J. Liu, *Energy Environ. Mater.*, 2022. DOI: 10.1002/eem2.12357.
9. Q. Zhang, X. Hou, X. Liu, X. Xie, L. Duan, W. Lu and G. Gao, *Small*, 2021, **17**, e2103091.
10. M. Chen, W. Zhou, A. Wang, A. Huang, J. Chen, J. Xu and C.-P. Wong, *J. Mater. Chem. A*, 2020, **8**, 6828-6841.
11. X. Li, D. Lou, H. Wang, X. Sun, J. Li and Y. N. Liu, *Adv. Funct. Mater.*, 2020, **30**, 2007291.
12. T. Wei, Y. Ren, Z. Li, X. Zhang, D. Ji and L. Hu, *Chem. Eng. J.*, 2022, **434**, 134646.
13. F. Mo, G. Liang, D. Wang, Z. Tang, H. Li and C. Zhi, *EcoMat*, 2019, **1**, e12008.
14. F. Mo, G. Liang, Q. Meng, Z. Liu, H. Li, J. Fan and C. Zhi, *Energy Environ. Sci.*, 2019, **12**, 706-715.
15. X. Zhu, C. Ji, Q. Meng, H. Mi, Q. Yang, Z. Li, N. Yang and J. Qiu, *Small*, 2022, **18**, e2200055.
16. G. Ji, R. Hu, Y. Wang and J. Zheng, *J. Energy Storage*, 2022, **46**, 103858.
17. H. Cui, H. Mi, C. Ji, F. Guo, Y. Chen, D. Wu, J. Qiu and H. Xie, *J. Mater. Chem. A*, 2021, **9**, 23941–23954.
18. C. Ji, D. Wu, Z. Liu, H. Mi, Y. Liao, M. Wu, H. Cui, X. Li, T. Wu and Z. Bai, *ACS Appl. Mater. Interfaces*, 2022, **14**, 23452–23464.
19. G. Lou, G. Pei, Y. Wu, Y. Lu, Y. Wu, X. Zhu, Y. Pang, Z. Shen, Q. Wu, S. Fu and H. Chen, *Chem. Eng. J.*, 2021, **413**, 127502.
20. Y. Wang, X. Wang, X. Li, X. Li, Y. Liu, Y. Bai, H. Xiao and G. Yuan, *Adv. Funct. Mater.*, 2020, **31**, 2008185.